Lattice dynamics in antimony and tellurium based phase-change materials

Faculté des Sciences - Université de Liège

&

Jülich Centre for Neutron Science (JCNS-2)

and Peter Grünberg Institute (PGI-4)

Année académique 2014-2015

Dissertation présentée par
Ronnie Ernst Simon
en vue de l'obtention du grade de
Docteur en Sciences

Abstract

Phase change materials exhibit significant contrasts in both optical reflectivity and electrical resistivity between an amorphous and a crystalline phase, a contrast utilized to distinguish between logical states for data storage devices. They are widely used as the active medium in optical devices like CD-RW, DVD and Bluray discs and are promising candidates for non-volatile electronic memories. In this thesis the lattice dynamics of phase change materials is investigated by means of phonon spectroscopy and Mössbauer spectroscopy.
The feasibility of nuclear forward scattering by the 68.7 keV nuclear resonance of ^{73}Ge was demonstrated and its suitability for the study of condensed matter was characterized. The Ge specific lattice dynamics are easily accessed in terms of the Lamb-Mössbauer factor, atomic displacement parameter and Debye temperature through temperature dependent measurements. Furthermore, in combination with a reference sample it is possible to determine the relative isomer shift from which one can conclude on the Ge valence state.
The densities of phonon states of the prototypical phase change material Sb_2Te_3 in the high pressure δ-phase were determined at room temperature using ^{121}Sb and ^{125}Te nuclear inelastic scattering. From the densities of phonon states it is concluded that in δ-Sb_2Te_3 ordinary covalent bonding is prevalent, in contrast to resonance bonding in the ambient pressure α-phase. The measurements show that simultaneous sample cooling to approximately 100 K is required in order to study the pressure dependence of lattice dynamics, i.e. anharmonicity, in the $1 - 20$ GPa pressure regime, relevant for phase change materials.
The element resolved lattice dynamics of the $SnSb_2Te_4$ phase change material in the amorphous, cubic and hexagonal phases were determined using ^{119}Sn,^{121}Sb and ^{125}Te nuclear inelastic scattering. The densities of phonon states reveal an acoustic hardening upon crystallization for all three elements characterized by an increase in speed of sound and Debye temperature. With the onset of resonance bonding upon crystallization, a softening of optical phonons for Sb and Te but not for Sn is observed suggesting that there might be no change in bonding mechanism for Sn. From the density of phonon states the vibrational entropy is determined.
The generalized density of phonon states of Ge-Sb-Te phase change materials in the as deposited and cubic phases were determined using inelastic X-ray scattering by powder samples. A simultaneous hardening in the acoustic and softening in the optical phonon range is revealed, in line with previous nuclear inelastic and inelastic neutron scattering studies. By combining the inelastic X-ray with nuclear inelastic scattering data access to the Ge specific lattice dynamics was enabled. The Ge density of phonon states revealed high energy phonon modes that vanish upon crystallization and are most probably related to tetrahedrally coordinated Ge. Structural relaxation of the as deposited amorphous samples revealed no changes in vibrational properties.
The bonding properties of several phase change materials were investigated using ^{121}Sb Mössbauer spectroscopy. The Sb valence electron configuration determined from the isomer shift using tight binding calculations reveals a significant change in the number of Sb 5p electrons which relates to the onset of resonance bonding and the pronounced electron delocalization characteristic for this bonding mechanism. The results provide strong microscopic evidence for resonance bonding in crystalline phase change materials and establish ^{121}Sb Mössbauer spectroscopy as a fingerprinting technique for resonance bonding.

Kurzfassung

Phasenwechselmaterialien zeichnen sich durch einen hohen Kontrast in der optischen Reflektivität und dem elekrischen Widerstand zwischen einer amorphen und einer kristallinen Phase aus, welcher in Speichermedien zur Unterscheidung logischer Zustände verwendet wird. Phasenwechselmaterialien sind weit verbreitet als das aktive Medium in optischen Speichermedien wie CD-RW, DVD und Bluray Discs und vielversprechende Anwärter für nichtflüchtige elektronische Speichermedien. Die vorliegende Arbeit behandelt die Untersuchung von Phasenwechselmaterialien hinsichtlich ihrer gitterdynamischen Eigenschaften unter Verwendung von Phononenspektroskopie und Mössbauerspektroskopie.
Die Ausführbarkeit nuklearer Vorwärtstreuung am 68.7 keV angeregten Kernzustand von ^{73}Ge wurde gezeigt und deren Eignung zur Untersuchung von Festkörpern wurde dargestellt. Die Ge spezifische Gitterdynamik mit Hinblick auf Lamb-Mössbauer Faktor, atomaren Auslenkungsparameter und Debyetemperatur kann mittels temperaturabhängigen Messungen ohne größeren Aufwand untersucht werden. Des Weiteren kann in Verbindung mit einer Referenzprobe die Isomerieverschiebung bestimmt und Rückschlüsse auf die Ge Valenz gezogen werden.
Die Phononenzustandsdichte des prototypischen Phasenwechselmaterials Sb_2Te_3 in der δ-Phase wurde unter Hochdruck und bei Raumtemperatur mittels ^{121}Sb und ^{125}Te inelatischer Kernresonanzstreuung bestimmt. Der Vergleich der Zustandsdichten bei atmosphärischem und Hochdruck zeigt, dass in der δ-Phase kovalente Bindungen vorherrschen während in der α-Phase bei Raumdruck resonante Bindung zu beobachten ist. Die Messungen zeigen weiterhin, dass nur durch gleichzeitiges Kühlen der Proben auf etwa 100 K es möglich ist, die Druckabhängigkeit der Gitterdynamik, d.h. die Anharmonizität, im für Phasenwechselmaterialien relevaten Druckbereich von $1 - 20$ GPa zu untersuchen.
Die elementspezifische Gitterdynamik des Phasenwechselmaterials $SnSb_2Te_4$ in der amorphen, kubischen und hexagonalen Phase wurde mittels ^{119}Sn, ^{121}Sb und ^{125}Te unelastischer Kernresonanzstreuung bestimmt. Die Phononenzustandsdichten aller drei Elemente weisen eine akustische Erhärtung nach der Kristallisation auf, die sich in einem Anstieg der Schallgeschwindigkeit und Debye-Temperaturen widerspiegelt. Mit dem Einsetzen der Resonanzbindung bei der Kristallisation lässt sich eine Erweichung der optischen Sb und Te Moden jedoch nicht der Sn Phononen beobachten, was darauf hinweist, dass es keine Änderung des Bindungsmechanismus für Sn gibt. Aus den Phononenzustandsdichten wurde die Vibrationsentropie bestimmt.
Mittels unelastischer Röntgenstreuung an Pulverproben wurde die generalisierte Phononenzustandsdichte mehrerer Ge-Sb-Te Phasenwechselmaterialien in der amorphen und kubischen Phase bestimmt. In Übereinstimmung mit vorherigen Untersuchungen mittels unelastischer Kernresonanz- und Neutronenstreuung wurde eine gleichzeitige Erhärtung und Erweichung im Bereich der akustischen bzw. optischen Phononen festgestellt. Durch Kombination der Resultate von unelastischer Röntgenstreuung und Kernresonanzstreuung konnte die Ge spezifische Gitterdynamik erfasst werden. Die Ge Phononenzustandsdichte weist hochenergetische Phononenmoden auf, welche bei Kristallisation verschwinden und höchstwahrscheinlich mit tetraedrisch koordinierten Ge in Verbindung gebracht werden können. Nach struktureller Relaxation der amorphen Proben konnten keine Veränderungen gitterdynamischer Eigenschaften festgestellt werden.
Die Bindungseigenschaften verschiedener Phasenwechselmaterialien wurden mittels ^{121}Sb Mössbauerspektroskopie untersucht. Die Sb Valenzelektronenkonfiguration wurde anhand der Isomerieverschiebung mit Hilfe von Simulationen in der Näherung von stark gebundenen Elektronen

bestimmt und weist eine signifikante Änderung der Anzahl der Sb 5p-Elektronen auf, welche mit dem Einsetzen der Resonanzbindung und der dafür charakteristischen Elektronendelokalisierung zusammenhängt. Die Ergebnisse liefern starke Beweise für das Einsetzen der Resonanzbindung in der kristallinen Phase auf mikroskopischer Ebene und etablieren ^{121}Sb Mössbauerspektroskopie als Methode zur Identifizierung von Resonanzbindung.

Résumé

Les matériaux à changement de phase présentent d'importants contrastes en termes de réflectivité optique et de résistance électrique entre les phases amorphes et cristallines. Ce contraste est utilisé pour différencier des états logiques dans des dispositifs de stockage de données. Ces matériaux sont largement utilisés comme milieu actif dans des dispositifs optiques tels que les CD-RW, les DVD et les disques Blu-ray. Ils sont des candidats prometteurs pour les mémoires électroniques non volatiles. Dans cette thèse la dynamique de réseau des matériaux à changement de phase est étudiée par spectroscopie de phonon et spectroscopie Mössbauer.

L'applicabilité de mesures de diffusion nucléaire vers l'avant à la résonance nucléaire de 68.7 keV de ^{73}Ge et son aptitude à caractériser la matière condensée a été démontrée. Des quantités spécifiques de la dynamique de réseau, le facteur Lamb-Mössbauer, le paramètre de déplacement atomique et la température de Debye sont facilement accessibles par des mesures de la diffusion dépendante de la température. En outre, par l'utilisation d'un échantillon de référence, il est possible de déterminer le déplacement isomérique relatif, ce qui fournit une information direct sur l'état de valence de Ge.

La densité d'états de phonons du matériau à changement de phase prototypique Sb_2Te_3 sous haute pression et à température ambiante à été étudiée par la diffusion inélastique nucléaire de ^{121}Sb et ^{125}Te. La densité d'états de phonons permet de conclure que pour la phase δ-Sb_2Te_3, les liaisons covalentes sont dominantes. En revanche pour la phase α les liaisons résonantes sont dominantes à pression atmosphérique. Ces mesures montrent également que le refroidissement simultané de cet échantillon à environ 100 K est nécessaire pour étudier la dépendance en pression de la dynamique de réseau, c.à.d. de l'anharmonicité, dans le domaine de pression de 1 à 20 GPa, pertinent pour les matériaux à changement de phase.

Les caractéristiques principales de la dynamique de réseau du matériau à changement de phase $SnSb_2Te_4$ en phase amorphe, cubique et hexagonale à été étudié par diffusion inélastique nucléaire de ^{119}Sn, ^{121}Sb et ^{125}Te. La densité de phonons indique un durcissement acoustique lors de la cristallisation pour les trois éléments, caractérisés par une augmentation de la vitesse du son et de la température de Debye. Avec l'apparition de liaisons résonantes lors de la cristallisation un assouplissement des phonons optiques a été observé pour Sb et Te mais pas pour Sn, suggérant qu'il pourrait n'y avoir aucun changement dans le mécanisme de liaison pour Sn. L'entropie vibrationnelle a été déterminé à partir de la densité d'états de phonons.

La densité d'états de phonons des matériaux à changement de phase à base de Ge, Sb et Te dans en phase amorphe et cubique a été déterminé par diffusion inélastique de rayonnement synchrotron. Un durcissement acoustique accompagné d'un durcissement des phonons optiques est observé, en bon accord avec les études précédentes de diffusion nucléaire inélastique et diffusion inélastique de neutrons. L'accès à la dynamique de réseau spécifiques de Ge est possible par la combinaison des données de la diffusion inélastique de rayonnement synchrotron et de la diffusion nucléaire inélastique. La densité des états de phonons de Ge révèle des modes de phonons de haute énergie qui disparaissent lors de la cristallisation et qui sont très probablement liés à du Ge en coordination tétraédrique. Une relaxation structurale graduelle des échantillons amorphes ne conduit pas à un changement mesurable dans les propriétés vibratoires.

Les propriétés de liaison de plusieurs matériaux à changement de phase ont été étudiés par spectroscopie Mössbauer de ^{121}Sb. La configuration électronique de la couche de valence à été déterminé à partir du déplacement isomérique par l'utilisation de calculs en approximation "tight-binding". Les mesures indiquent un changement significatif dans la densité des électrons 5p de Sb lié à la mise en place de liaisons résonantes et qui démontrent le phénomène de délocalisation électronique pour ce mécanisme de liaison. Ces résultats fournissent des preuves microscopiques solides pour l'existence de liaisons résonantes dans les matériaux à changement de phase en phase cristalline et montrent que la spectroscopie Mössbauer de ^{121}Sb est une technique d'empreinte très sensible pour l'étude des liaisons résonantes.

Acknowledgements

I would like to express my deep gratitude to Prof. Raphaël P. Hermann for his supervision of my thesis. I am very grateful for his patience, guidance, motivation, enthusiasm and advice throughout my research tenure. He has been actively interested in my work and has taught me so many things. Thanks to him I was also able to travel to various places and experience new countries and cuisines.

I would like to thank my co-advisor at the Université de Liège Prof. Rudi Cloots, Prof. Bénédicte Vertruyen, Prof. Matthieu Verstraete and Prof. Manuel Angst for being members of the thesis jury. I am grateful to Dr. Pierre-Emmanuel Lippens and Prof. Matthias Wuttig for accepting to be the external referees of my doctoral thesis.

Many people helped me to realize this work and I would like to thank all of them. Jens Gallus is acknowledged for collecting the experimental data during his master's thesis on the $SnSb_2Te_4$ phase change material. I am very grateful to Dr. Ilya Sergueev for his great efforts in teaching me about nuclear resonance scattering and his invaluable support. I very much appreciate Dr. Benedikt Klobes for all his support in- and outside of the laboratory and the many fruitful discussions. He was always a source of advice and provided help in numerous ways not only scientifically. It gives me great pleasure to acknowledge Dr. Abdelfattah Mahmoud for the discussions about the Mössbauer spectroscopy results of this thesis. I gained a lot from his chemistry knowledge. I would like to thank Dr. Vasily Potapkin for his advices, especially concerning high pressure techniques. I am also indebted to Jörg Perßon for his help in the chemistry laboratory and the sample preparation. I express my gratitude to Berthold Schmitz and Frank Gossen for their technical support no matter how busy they were. Special thanks also go to all the members of our group who helped me with many measurements and during beam times, Marcus Herlitschke, Atefeh Jafari, Pavel Alexeev, Mikheil Mebonia, Thomas Könen, Paula Bauer Pereira and Tania Claudio Weber. I would like to thank Felix Lange, Stefan Jakobs and Karl Simon Siegert for all the fruitful discussions and their efforts they put into the sample preparations. My sincere thanks go to Dr. Rudolf Rüffer for offering me the internship opportunity at beamline ID18 of the European Synchrotron Radiation Facility. I am also very grateful to Prof. Thomas Brückel for giving me the opportunity to perform my doctoral studies in the Jülich Centre for Neutron Science.
I was fortunate to share an office with Johannes Reim and Markus Schmitz and I thank you for the joyful atmosphere in the office, for all the fun we had on so many occasions such as conferences, during lunches, coffee breaks, Christmas seasons, day9 presentations, sandwich sessions, for your musical interludes and all the other memories that we created together. I would also like to thank all the other wonderful people in our institute for making my PhD thesis memorable in so many ways.
The German research foundation is acknowledged for the financial funding of my doctoral thesis within the special research program SFB917 Nanoswitches of the RWTH Aachen University and the Forschungszentrum Jülich GmbH. The European Synchrotron Radiation Facility (ESRF) and the Deutsches Elektronen-Synchrotron (DESY) are acknowledged for the provision of beam time. Many thanks go to all the people working at the beam lines at the European Synchrotron Radiation Facility (ESRF) Dr. R. Rüffer, Dr. A. Chumakov, Dr. D. Bessas and at the Deutsches Elektronen-Synchrotron (DESY) Dr. H. C. Wille and Dr. K. Schlage for their technical assistance. Their support is invaluable.

I am grateful to all my friends who provided welcome distractions whenever necessary. Finally, I want to thank my loving parents and my dear girlfriend, Jessica, for their constant love and support.

Contents

Chapter 1

1 Introduction

The progress of mankind has always been driven by the possibility to store and exchange information. The evolution of techniques for data storage reaches from prehistoric wall carvings over the invention of printing to highly sophisticated solid state memories, for example. Nowadays, new memory devices are demanded that comprise large storage capacities, fast read and write speeds and long data retention. Furthermore, energy efficiency, scalability and mobility are becoming more and more crucial.

Phase change materials exhibit a rich portfolio of unusual properties rendering them a unique class of materials and ideal for storage devices. In the following a brief overview of the properties and applications of phase change materials is given. For further details, the reader is referred to the comprehensive review articles, Refs. [1–4], which have been used to compose this chapter.

The key features of phase change materials are a significant contrast in electronic properties, namely the optical reflectivity and the electrical resistivity, between an amorphous and a metastable crystalline phase and the possibility to switch reversibly and fast between the two phases. The property contrasts are utilized in order to distinguish between logical states to store information. Phase change materials are well established as the active medium in optical storage devices since the invention of the rewritable compact disc CD-RW in 1996. The recording layers of present-day optical discs like the digital versatile disc (DVD), in particular DVD random access memory (DVD-RAM) and DVD±RW, and the Blu-ray disc are also based on phase change materials. Furthermore, phase change materials are promising candidates for non-volatile electronic memories which combine the fast read and write speeds of the dynamic random access memory and the non-volatility of the Flash memory.

The principle of operation of a phase change material based memory device is the following. Heat is supplied to an amorphous region of phase change material in order to trigger crystallization. Re-amorphization of the crystalline region is achieved by supplying heat in sufficiently large amount such that the material is locally melted. If the melted material is subsequently cooled down sufficiently fast that the atoms have no time to rearrange the structure of the amorphous phase is retained. The source of heat can either be a laser pulse, as used in optical storage devices, or a current pulse, as used in electronic memories. Information is read out, *i.e.* probing whether the material is in the amorphous or crystalline phase, by applying a laser or current pulse with sufficiently low power such that the material is neither amorphized nor crystallized.

The most prominent phase change materials are the pseudo binary compounds $(GeTe)_{1-x}(Sb_2Te_3)_x$ and among those $Ge_2Sb_2Te_5$ ($x = 1/3$) and $Ge_8Sb_2Te_{11}$ ($x = 1/9$) are used for DVD-RAM [5] and Blu-ray discs [6], respectively. Compounds that show phase change behaviour are also found in the Sn-Sb-Te system which is isovalent to Ge-Sb-Te, for example $SnSb_2Te_4$. Sb_2Te compounds doped to large amount with In and Ag are also used as phase change materials and a stoichiometry close to $Ag_5In_5Sb_{60}Te_{30}$, known as AIST, is utilized in DVD±RW discs [7]. Another group of materials

that show phase change behaviour are InSb-InTe pseudo binary alloys such as In_3SbTe_2 [8].
Most phase change materials crystallize in an octahedral-like atomic arrangement and, for example, Ge-Sb-Te phase change materials in the metastable crystalline phase exhibit a distorted rocksalt like structure, where Te occupies the anion sublattice and Ge, Sb and vacancies randomly occupy the cation sublattice. Though considered as defects in a crystal structure, the vacancies in phase change materials actually stabilize the crystalline phase [9] and are thus considered as an intrinsic feature of the structure. For $(GeTe)_{1-x}(Sb_2Te_3)_x$ the concentration of vacancies on the second sublattice is given by $(1 - x)/(3 - 2x)$. For example, in $GeSb_2Te_4$ with $x = 1/2$ there are 25 % vacancies present.
An outstanding property of phase change materials is a change in the bonding mechanism upon crystallization which is closely related to functional properties of phase change materials. Whereas ordinary covalent bonding is present in the amorphous phase, the crystalline phase exhibits resonance bonding [10]. The concept of resonance bonding was introduced by Linus Pauling in 1939 [11]. A famous example for resonance bonding is the benzene molecule. Its structure is a six-membered ring of carbon atoms with alternating single and double bonds between them. Each carbon atom is in addition bonded to an hydrogen atom. The true state of the molecule must be considered as a superposition of two energetically equivalent configurations of distributing the double bonds around the ring. Due to the superposition the electrons of the double bond are delocalized over the ring, thus lowering the energy of the system.
In phase change materials a similar superposition of bonding configurations occurs. In crystalline phase change materials with octahedral-like atomic configuration the atoms are bonded via p-electrons. In Ge-Sb-Te compounds, for example, there are on average three p-electrons per atom, however, the atoms can bond to six octahedral neighbours. Thus, different bonding configurations of one atom bonding to three neighbours are possible. Resonance bonding is formed by the superposition of all possible bonding configurations which results in a delocalization of the three p-electrons over all six bonds. Due to the delocalization of electrons phase change materials exhibit an increased electronic polarizability in the crystalline state which is the origin for the increased optical reflectivity [10].
Next to the optical contrast resonance bonding is also the reason for the rather low thermal conductivity of crystalline phase change materials and softening of optical phonon modes upon crystallization [12, 13]. The low thermal conductivity of phase change materials is of particular importance as it determines the actual size of an amorphous region after melting the material and thus the storage capacity of a device. Furthermore, the thermal power necessary to melt the material decreases with decreasing thermal conductivity, thus improving the energy efficiency.
The subject of this thesis is the investigation of vibrational properties of phase change materials. As macroscopic thermodynamical properties like heat capacity, thermal conductivity and speed of sound are determined by the vibrational movement of atoms, knowledge of the lattice dynamics is crucial for a deep understanding of the microscopic mechanisms underlying the functional properties of phase change materials. Within the scope of this thesis a two-pronged approach has been undertaken to study lattice dynamics of phase change materials, on the one hand, by phonon spectroscopy for probing the density phonon of states and, on the other hand, by Mössbauer spectroscopy for probing bonding properties, as the bonding of atoms defines the framework in which the atoms can vibrate.
The thesis is organized as follows. In Chapter 2, an introduction into the experimental methods applied within the scope of this thesis is given. This chapter should be considered as a brief overview

of the experimental techniques and for a comprehensive description the reader is referred to according literature.
Chapters 3 and 4 are devoted to further developments of the nuclear resonance scattering technique. Chapter 3 as presented in this thesis was published in the journal Europhysics Letters, 104, 17006 in 2013. This chapter is about the first application of nuclear forward scattering to the 68.7 keV nuclear resonance of ^{73}Ge in a series of Ge reference compounds in order to, first, demonstrate its feasibility in general and, second, to characterize its suitability for the study of solid state physics and lattice dynamics, in particular. These studies must be considered as a prerequisite for future investigations of phase change material using ^{73}Ge nuclear forward scattering. The relevance of such investigations is underlined by the ^{121}Sb Mössbauer spectroscopy results presented in Chapter 7 of this thesis.
Chapter 4 as presented in this thesis was published as an invited contribution in the journal Semiconductor Science and Technology, 29, 124001 in 2014. In this chapter the results of pressure dependent phonon spectroscopy measurements carried out for the first time using ^{121}Sb and ^{125}Te nuclear inelastic scattering by the prototypical phase change material Sb_2Te_3 are presented.
The thesis continues with a lattice dynamical study of the $SnSb_2Te_4$ phase change material in Chapter 5. ^{119}Sn, ^{121}Sb and ^{125}Te nuclear inelastic scattering are used to determine the element resolved lattice dynamics of the amorphous, metastable cubic and stable hexagonal phase of $SnSb_2Te_4$.
Chapter 6 comprises the investigation of Ge-Sb-Te phase change materials in the amorphous and metastable crystalline phase using inelastic X-ray scattering. In combination with previous nuclear inelastic scattering studies the Ge specific lattice dynamics are accessed.
In Chapter 7, the results of ^{121}Sb Mössbauer spectroscopy studies on a series of different families of phase change materials are presented. These studies focus on the investigation of the bonding properties in phase change materials from the Sb perspective on a microscopic scale and, in particular, on the impact of the change in bonding mechanism upon crystallization on the Sb electron configuration. Finally, a summary and an outlook are given in Chapter 8.

Chapter 2

2 Experimental methods

In the following a brief introduction of the experimental methods used within the scope of this thesis is given. For further details the reader is referred to corresponding literature which is given for each technique.

2.1 Mössbauer spectroscopy

Mössbauer spectroscopy is a technique used to measure the energy of nuclear transitions between a ground and an excited nuclear state with very high precision giving access to information about the local structural, chemical and magnetic environment of Mössbauer active nuclei. A comprehensive overview of Mössbauer spectroscopy can be found for example in Ref. [14] and only a brief description of the technique is given in the following.

Mössbauer spectroscopy is based on the recoil-free emission and resonant absorption of γ-rays by atomic nuclei. The concept of nuclear resonance absorption is shown schematically in Figure 2.1. A nucleus in an excited state populated by the radioactive decay of a parent isotope or by absorption of radiation undergoes a transition to the ground state via the emission of a photon. This photon is subsequently absorbed by a second nucleus of the same type as the energy of the photon matches the energy of the nuclear transition.

Considering conservation of energy and momentum, however, the emission and absorption of a photon must be associated with a recoil acting on the nucleus. Thus, for a free nucleus the energy of the emitted photon is lower than the energy of the nuclear transition and subsequent resonant absorption can only take place if the photon energy is larger than the energy of nuclear transition in order to compensate for the recoil. Hence, for free nuclei nuclear resonant absorption cannot take place as the recoil is so large that there is no overlap in energy between the emission and absorption lines.
Rudolf Mössbauer discovered that if the nuclei are bound in a solid there is a finite probability for recoil-*free* emission and absorption of photons such that nuclear resonant absorption can occur, a process known as the Mössbauer effect [15–17]. Within the solid the recoil associated with the emission or absorption is not taken up by the nucleus itself but by the whole crystal lattice such that lattice vibrations, *phonons*, are created or annihilated. However, there is a finite probability for recoil-free emission and absorption of γ-rays, *i.e.* without creating or annihilating a phonon,

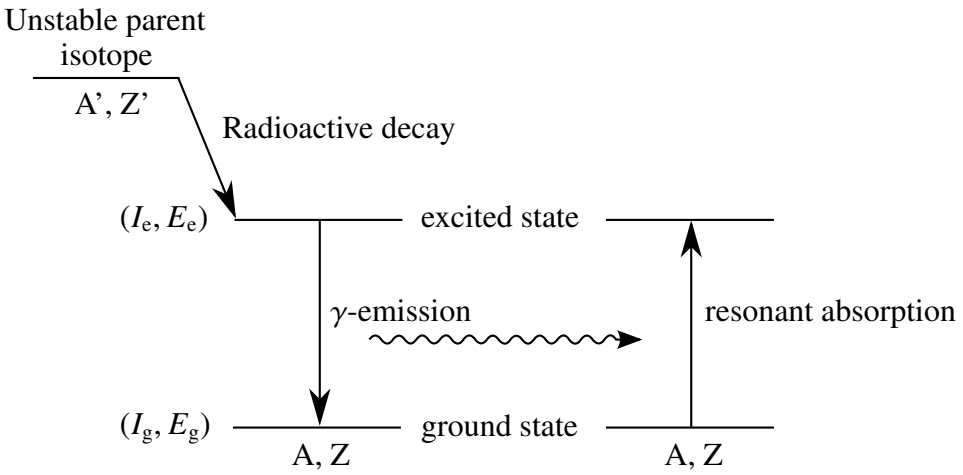

Figure 2.1: Concept of nuclear resonant absorption. The excited state of a nucleus with mass A and charge Z populated via the radioactive decay of a parent isotope decays via the emission of a photon to the ground state. This photon is subsequently absorbed by a nucleus of the same type. $I_{g,e}$ and $E_{g,e}$ are nuclear spin and energy of the ground and excited state, respectively. The drawing is adapted from Ref. [14].

which is given by the Lamb-Mössbauer factor

$$f_{\mathrm{LM}} = \exp\left(-\frac{\langle u^2\rangle\, E_\gamma^2}{\hbar^2 c^2}\right), \tag{2.1.1}$$

where $\langle u^2\rangle$ is the mean square atomic displacement parameter, E_γ is the γ-ray energy, $\hbar$ is the reduced Planck constant and c is the speed of light. As the mean square atomic displacement parameter increases with increasing temperature, higher temperatures yield a lower Lamb-Mössbauer factor. In the Debye approximation, the temperature dependence of the Lamb-Mössbauer factor is given by [14]

$$f_{\mathrm{LM}}(T) = \exp\left[\frac{-3E_\gamma^2}{k_B\theta_{\mathrm{D}}Mc^2}\left\{\frac{1}{4} + \left(\frac{T}{\theta_{\mathrm{D}}}\right)^2 \int_0^{\frac{\theta_{\mathrm{D}}}{T}} \frac{x}{e^x - 1}dx\right\}\right], \tag{2.1.2}$$

where T is the temperature, k_B is the Boltzmann constant, θ_{D} is the Debye temperature and M is the mass of the nucleus. In Figure 2.2, the temperature dependence of the Lamb-Mössbauer factor for the Mössbauer isotope ^{121}Sb is shown for different Debye temperatures.

A typical experimental setup for Mössbauer spectroscopy is shown in Figure 2.3. The radioactive Mössbauer source is attached to a so-called Mössbauer drive moving the source with variable velocity in order to tune the energy of the emitted γ-radiation utilizing the Doppler effect. The velocity is thereby linearly increased and decreased by applying an appropriate modulation voltage, for example with triangular shape. For the Mössbauer isotope ^{121}Sb the spectrum is typically recorded within a velocity range of $\pm 30\,\mathrm{mm/s}$. As the γ-ray spectrum of the Mössbauer source does not only contain photons from the relevant Mössbauer transition a pulse height discrimina-

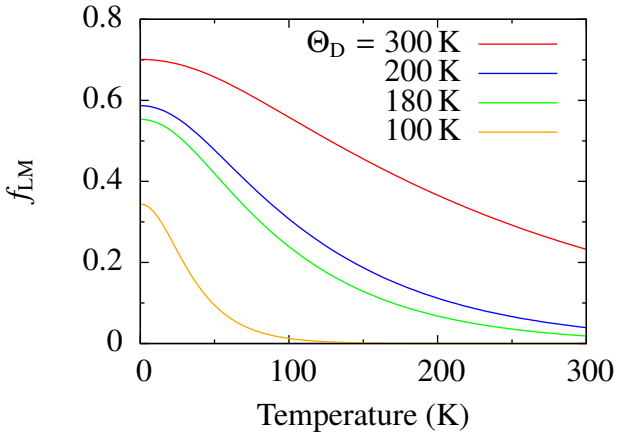

Figure 2.2: Lamb-Mössbauer factor, f_{LM}, as a function of temperature calculated in the Debye approximation, see Eq. (2.1.2), for the Mössbauer isotope ^{121}Sb for different Debye temperatures given in the graph. The Debye temperature of elemental Sb is 180(5) K [18].

tion is performed using a single channel analyser (SCA) in order to exclude those. A typical pulse height spectrum of ^{121m}Sn used for ^{121}Sb Mössbauer spectroscopy and recorded with a NaI scintillation detector is shown Figure 2.3. The spectrum reveals the Mössbauer transition, Sb K_α X-ray fluorescence and an iodine escape peak [19]. For ^{121}Sb Mössbauer spectroscopy the windows of the SCA are set to the energy of the Mössbauer transition and to that of the iodine escape peak. The full Mössbauer transmission spectrum is acquired using a multi-channel analyser (MCA) which is synchronized with the Mössbauer drive such that each channel corresponds to a certain velocity range. The velocity scale of the spectrometer is calibrated using a ^{57}Co source and α-Fe sample at room temperature.

The Mössbauer transition of ^{121}Sb is a M1 magnetic dipole transition between the 5/2+ ground and the 7/2+ first excited state with an energy of 37.13 keV and a half life of 3.46 ns [20]. Due to the half life of the excited state the natural line width of the Mössbauer transition is relatively large with 2.1 mm/s in terms of the corresponding Doppler velocity [20]. The nuclear quadrupole moments of the 5/2 and 7/2 states are −0.36(4) b and −0.48(5) b, respectively, and the nuclear magnetic moments are 3.3634(3) μ_N and 2.518(7) μ_N, respectively [20]. The ^{121}Sb Mössbauer spectroscopy measurements in this thesis were performed with a $Ca^{121m}SnO_3$ source at room temperature. The decay scheme of ^{121m}Sn is shown in Figure 2.4.a. The excited state of the ^{121}Sb Mössbauer transition is populated through β^- decay of the 3/2+ state of ^{121m}Sn with a half life of 44 y and a branching ratio of 22.4 %. With a branching ratio of 77.6 % the 3/2+ state decays to the 11/2- state of ^{121m}Sn via internal conversion which subsequently solely decays via a β^- decay to the 5/2+ ground state of ^{121}Sb.

2.2 Nuclear interactions

In Mössbauer spectroscopy the interaction of nuclei with electric and magnetic fields is utilized in order to study the local environment of the Mössbauer nuclei. The nuclear interactions relevant for

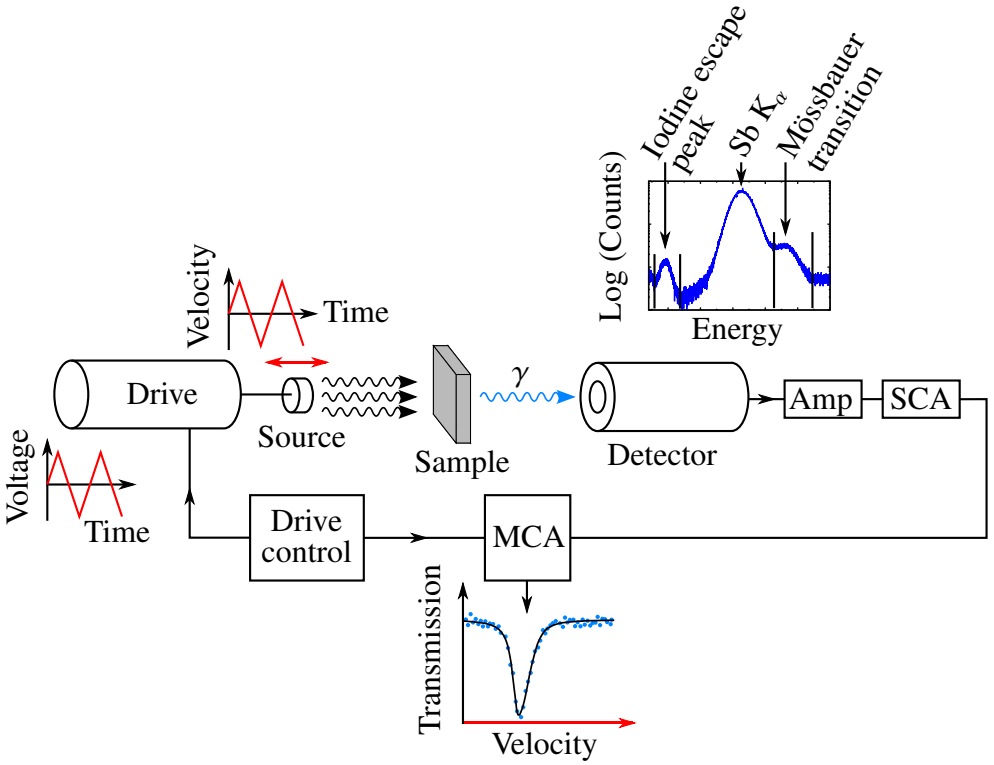

Figure 2.3: Typical experiment setup for Mössbauer spectroscopy. A radioactive source containing the Mössbauer isotope is moved by the drive with increasing and decreasing velocity determined by the modulation voltage provided by the drive control. The signal from the detector measuring the transmission of γ-radiation through the sample is amplified (AMP) and analysed by means of a pulse height discrimination using a single channel analyser (SCA) in order to record only photons originating from the Mössbauer transition. A typical pulse height spectrum of the ^{121m}Sn source recorded with a NaI scintillation detector is shown revealing the ^{121}Sb Mössbauer transition, Sb K_α X-ray fluorescence and an iodine escape peak [19]. For ^{121}Sb Mössbauer spectroscopy the energy windows of the SCA are set to the energy of the Mössbauer transition and to that of the iodine escape peak. The full Mössbauer transmission spectrum is acquired using a multi channel analyser (MCA) which is synchronized with the drive control such that each channel of the MCA corresponds to a certain velocity range. The drawing is adapted from Ref. [14].

Mössbauer spectroscopy are: the isomer shift, the electric quadrupole splitting and the magnetic splitting [14]. In the following, the three different interactions will be briefly introduced following Ref. [14].

2.2.1 Isomer shift

The isomer shift is related to the interaction of the electronic charge density of the Mössbauer atom at the nucleus with the nuclear charge distribution of the nucleus itself resulting in energy changes of the nuclear states. As different nuclear states have different nuclear charge distributions

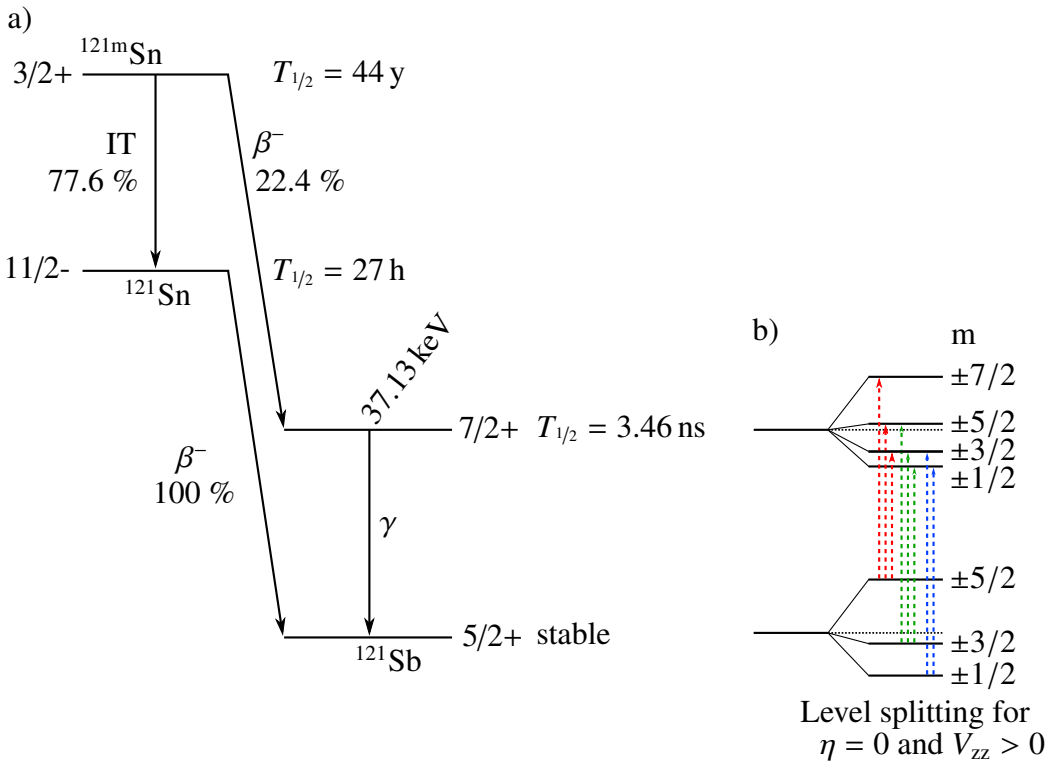

Figure 2.4: a) Decay scheme of ^{121m}Sn and the 7/2+ to 5/2+ Mössbauer transition of ^{121}Sb. Half lives, $T_{1/2}$, and branching ratios of internal conversion (IT) and β^- decay are given in the figure. Values are taken from Ref. [20]. b) Level splitting of the 5/2+ and 7/2+ states with respect to the magnetic quantum number, m, due to electric quadrupole interaction in case of an asymmetry parameter, $\eta = 0$, and a positive electric field gradient, V_{zz}. The eight transitions allowed by the selection rules for a M1 transition, $\Delta m = 0, \pm 1$, are also shown.

the states are shifted differently which, in turn, results in a change in energy of the Mössbauer transition. Assuming the nucleus to be a positively charged sphere of radius R the energy of the Mössbauer transition is given by [14]

$$E_\gamma = E_0 + \frac{2\pi}{5} Z e^2 |\Psi(0)|^2 \left(R_e^2 - R_g^2\right) \tag{2.2.1}$$

where E_0 is the energy of the Mössbauer transition without the interaction, Z is the charge number of the nucleus, $-e|\Psi(0)|^2$ is the electronic charge density at the nucleus and $R_{g,e}$ are the radii of the nucleus in the ground and excited state, respectively. As the chemical bonding of a Mössbauer atom to its surrounding influences the electronic charge density, E_γ depends on the specific bonding configuration, see Figure 2.5. The difference in E_γ between the sample (absorber) and the source or any other reference is called the isomer shift

$$\delta = \frac{2\pi}{5} Z e^2 \left(|\Psi(0)|_A^2 - |\Psi(0)|_S^2\right)\left(R_e^2 - R_g^2\right), \tag{2.2.2}$$

where $-e|\Psi(0)|^2_{A,S}$ are the electronic charge densities at the nucleus in the absorber (A) and source (S), respectively. The isomer shift can be used to distinguish between different valence states of the

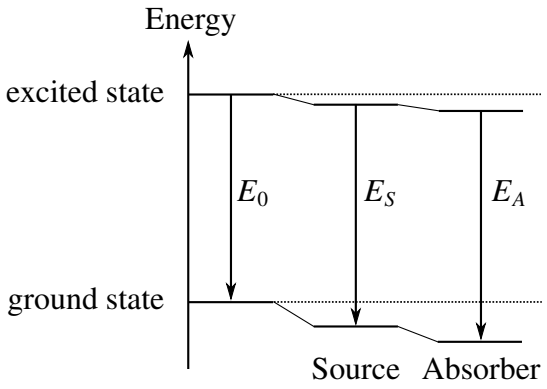

Figure 2.5: The interaction of the nuclear charge distribution of the Mössbauer nucleus with the electronic charge density at the nucleus causes a change in energy of the transition between the excited and ground state which is different in the source and the absorber due to the chemical bonding of the Mössbauer atom. The resulting difference $\delta = E_A - E_S$ is called the isomer shift. The figure is adapted from Ref. [14].

Mössbauer atom. In particular, for ^{121}Sb linear relations exist [21] between the valence electron density at the nucleus, the number of Sb 5s electrons and the isomer shift, see Figure 2.6. In addition, the number of Sb 5p electrons can be determined from the following empirical formula [21]:

$$\rho_{\mathrm{v}}(0) = 0.11 + 68.65N_{\mathrm{s}} - 3.39N_{\mathrm{p}} - 5.57N_{\mathrm{s}}^2 - 1.00N_{\mathrm{s}}N_{\mathrm{p}}. \tag{2.2.3}$$

Thus, measuring the isomer shift allows one to estimate the Sb valence electron configuration.

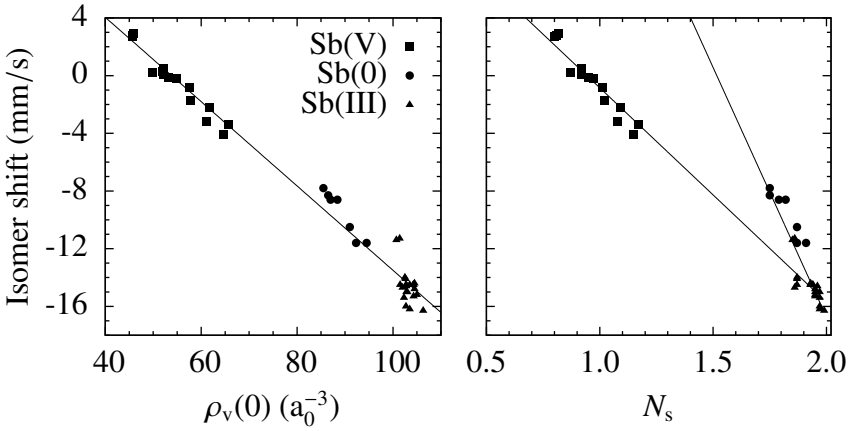

Figure 2.6: Valence electron density $\rho_{\mathrm{v}}(0)$ at the nucleus and number of Sb 5s electrons, N_{s}, as function of the isomer shift for compounds with different Sb valence states (0, III, V). a_0 is the Bohr radius. Lines are linear fits to the data. Data are taken from Ref. [21].

Experimentally, the measured isomer shift, δ_{exp}, in general consists of the genuine isomer shift, δ, and a relativistic contribution, the second order Doppler shift, δ_{SOD}, associated with a shift in energy due to thermal motion of the nuclei.

$$\delta_{\mathrm{exp}} = \delta + \delta_{\mathrm{SOD}} \tag{2.2.4}$$

The genuine isomer shift, δ, is temperature independent. However, as the magnitude of the thermal motion is temperature dependent, the measured isomer shift exhibits a temperature dependence which has to be corrected for when comparing values measured at different temperatures. The second order Doppler shift, in general, is given by [14]

$$\delta_{\mathrm{SOD}} = -E_\gamma \frac{\langle v^2 \rangle}{c^2}, \tag{2.2.5}$$

where $\langle v^2 \rangle$ is the mean squared velocity the atom is vibrating with. In the Debye model, the second order Doppler shift is given by [14]

$$\delta_{\mathrm{SOD}} = -\frac{9 k_{\mathrm{B}} E_\gamma}{16 M_{\mathrm{eff}} c^2} \left(\Theta_{\mathrm{M}} + 8T \left(\frac{T}{\Theta_{\mathrm{M}}} \right)^3 \int_0^{\Theta_{\mathrm{M}}/T} \frac{x^3}{\mathrm{e}^x - 1} dx \right), \tag{2.2.6}$$

where k_{B} is the Boltzmann constant, E_γ the Mössbauer transition energy, M_{eff} is the effective mass of the vibrating atom, c is the speed of light, Θ_{M} is the Mössbauer temperature in analogy to the Debye temperature but specific for the local environment of the Mössbauer nucleus and T is the temperature.

2.2.2 Quadrupole splitting

The interaction of the nuclear quadrupole moment, Q, with the electric field gradient at the nucleus caused by the electrons of the Mössbauer atom and the charges of surrounding atoms results in a change in energy of the nuclear states. A non-vanishing electric field gradient arises from a non-cubically symmetric charge distribution around the nucleus. Thus, the electric field gradient can provide information about the local symmetry of the site of the Mössbauer atom and about bonding properties. The electric field gradient, V_{ij}, is the second derivative of the electric potential, V, and can be described as a 3 x 3 second-rank tensor

$$V_{ij} = \frac{\partial^2 V}{\partial x_i \partial x_j}. \tag{2.2.7}$$

Due to the symmetry of the tensor the electric field gradient can be diagonalized by choosing a proper principal axis system. By convention, the principal axis system is chosen such that $|V_{zz}| \geq |V_{yy}| \geq |V_{xx}|$. Laplace's equation further requires the electric field gradient to be traceless

$$0 = V_{xx} + V_{yy} + V_{zz} \tag{2.2.8}$$

Thus, only two parameters are necessary to describe the electric field gradient. Usually, the largest component of the electric field gradient, V_{zz}, and the asymmetry parameter defined as $\eta = \frac{V_{xx} - V_{yy}}{V_{zz}}$

are chosen. In the case of $\eta = 0$ the energy of the quadrupole interaction is given by

$$E_{\mathrm{Q}}(I, m) = \frac{eQV_{zz}}{4I(2I-1)}\left(3m^2 - I(I+1)\right). \tag{2.2.9}$$

Hence, the presence of a non-vanishing electric field gradient removes the degeneracy in energy of the nuclear states with respect to the modulus of the magnetic quantum number, m. The parameter $eQV_{zz}/2$ is called the quadrupole splitting. In Figure 2.4.b, the splitting of the ground and excited states of the ^{121}Sb Mössbauer transition is shown together with the eight allowed transitions between nuclear substates according to the selection rules for the M1 magnetic dipole transition.

2.2.3 Magnetic splitting

Similar to the quadrupole splitting, the nuclear magnetic dipole moment of the nucleus can interact with a magnetic field at the nucleus giving rise to a change in energy of the nuclear levels according to

$$E_{\mathrm{M}} = -g_{\mathrm{N}}\mu_{\mathrm{N}}Bm, \tag{2.2.10}$$

where g_{N} is the Landé factor, μ_{N} is the nuclear magneton and B is the magnetic field strength. The interaction of the nucleus with a magnetic field completely lifts the degeneracy of the nuclear levels in energy with respect to the magnetic quantum number, m. This interaction is of no further relevance for this thesis.

2.3 Nuclear resonance scattering

Nuclear resonance scattering utilizes synchrotron radiation in order to excite the Mössbauer transition of Mössbauer active nuclei. The basic setup of a nuclear resonance scattering beam line at a synchrotron is shown in Figure 2.7. The X-ray radiation coming from the undulator is monochromatized in two steps, first by a high heat load monochromator to a few eV bandwidth and second by a high resolution monochromator to a few meV bandwidth or less. A high energy resolution is required particularly for phonon spectroscopy employing nuclear inelastic scattering (NIS), see below, and is also necessary in order to reduce the high intensity of the synchrotron radiation for protection of the detectors. The intensity of the radiation is monitored using an ionization chamber in front of the sample.
The radiation scattered from the sample must be analysed in time in order to separate electronic scattering and fluorescence from nuclear scattering. The nuclear scattering is delayed in time due to the finite life time of the excited state, which is on the order of ns to μs. On that time scale the electronic scattering occurs promptly after the synchrotron pulse has impinged on the sample. Therefore, signals measured in the first few ns after the synchrotron pulse are rejected.
The nuclear scattering measured in forward direction far away from the sample gives the nuclear forward scattering signal, see Chapter 2.3.1, whereas the X-ray and nuclear fluorescence of the sample measured closed to it and perpendicular to the beam direction gives the nuclear inelastic scattering signal, see Chapter 2.3.2.

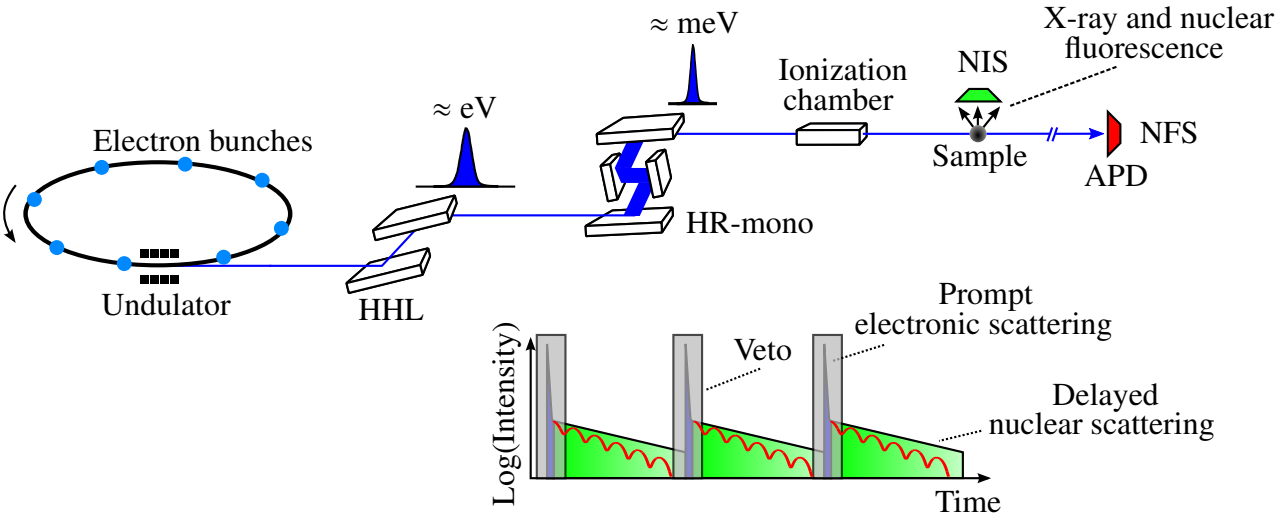

Figure 2.7: Basic setup of a nuclear resonance scattering beam line at a synchrotron. When the electron bunches pass through the undulator they emit synchrotron radiation which is subsequently monochromatized in two steps by a high heat load monochromator (HHL) to a few eV and by a high resolution monochromator (HR-mono) to a few meV. The intensity of radiation impinging on the sample is monitored using an ionization chamber. Silicon avalanche photodiode detectors (APD) are used to measure the nuclear forward scattering (NFS) and nuclear inelastic scattering (NIS) signal. The NIS signal is recorded by detecting the X-ray and nuclear fluorescence emitted by the sample after the decay of the excited Mössbauer nuclei via internal conversion. In both NFS and NIS the measured signal is analysed in time in order to separate the prompt electronic from the delayed nuclear scattering. Signals recorded in the first few ns after the synchrotron pulse are therefore rejected (Veto).

2.3.1 Nuclear forward scattering

A comprehensive introduction into nuclear forward scattering can be found in Ref. [22] and only a brief description of the basic principles is given in the following.

Nuclear forward scattering can be considered as the time-analogue to conventional Mössbauer spectroscopy which is performed in the energy domain, yet there are important differences. Whereas in Mössbauer spectroscopy the source of radiation is a radioactive isotope decaying via the Mössbauer transition with an energy resolution determined by the transition's natural linewidth, in nuclear forward scattering synchrotron radiation with an energy resolution determined by the crystal monochromators is used. The energy width of the synchrotron radiation used in nuclear forward scattering is typically on the order of 1 meV which is sufficiently large to excite all possible transitions between the nuclear substates with respect to the magnetic quantum number m, as shown in Figure 2.8. When a synchrotron pulse impinges on an ensemble of Mössbauer nuclei there is a finite probability amplitude for each nucleus of the ensemble to be excited into one of the possible nuclear substates. However, it cannot be distinguished which nucleus was excited into which nuclear substate. Thus, the resulting quantum state of the ensemble of nuclei is a superposition of all possible states of excitation each with a finite probability amplitude. When the ensemble

subsequently decays via the emission of photons with slightly different energies according to the specific nuclear transition, all these possible states of excitation interfere with each other. In time domain this interference is visible as a periodic modulation of the exponential decay curve with the half life of the excited state. From the modulation period information about the difference in energy between the substates, that is the strength of hyperfine interactions, see Chapter 2.2, is obtained. If no hyperfine interactions are present the resulting time spectrum is simply given by an exponential decay curve in case of a thin sample. For thick samples multiple scattering, see below, can lead to a similar modulation in time.
It is important to note that, whereas in Mössbauer spectroscopy the Mössbauer source is an intrinsic reference for the isomer shift, in nuclear forward scattering the determination of the isomer shift requires a specific reference sample and the time spectrum of the reference and the sample together must be recorded.

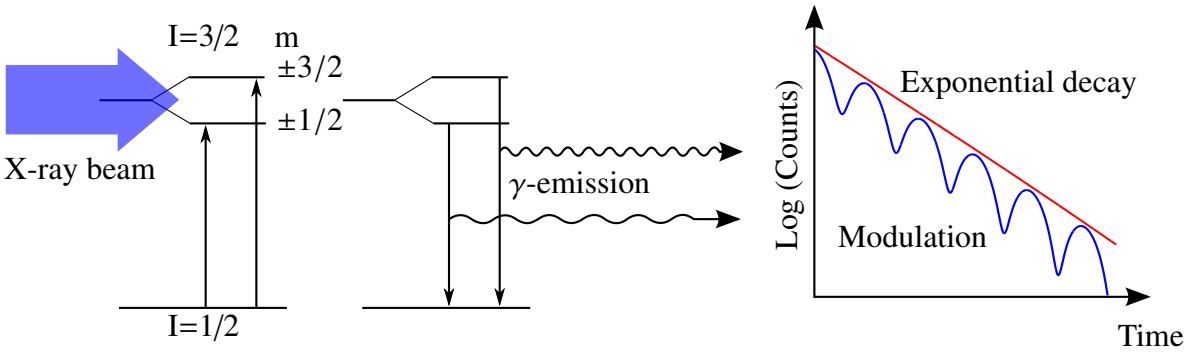

Figure 2.8: Basic principle of nuclear forward scattering using the example of a transition from a ground state with spin $I = 1/2$ to an excited state with spin $I = 3/2$. The excited state is splitted in energy with respect to the modulus of the magnetic quantum m, as can result from quadrupole interaction. The energy width of the incoming X-ray beam is sufficiently large that both possible transitions can be excited. Considering an ensemble of nuclei, it cannot be distinguish which nucleus was excited into which state and the resulting excited state of the ensemble is a superposition of all possible states of excitations. When the ensemble decays via the emission of photons with slightly different energies all these possible states interfere such that a periodic modulation of the exponential decay curve is observed.

Next to hyperfine interactions also multiple scattering can lead to time-modulations of the nuclear forward scattering time spectrum with a frequency which depends on the effective thickness of the sample given by [22]

$$\xi = \frac{1}{4} L \frac{\beta}{V} \sigma_0 f_{\mathrm{LM}}, \tag{2.3.1}$$

where L is the sample thickness, β is the isotopic enrichment factor in the Mössbauer isotope, V is the volume per Mössbauer atom and σ_0 is the nuclear resonant absorption cross section. If no hyperfine interactions are present the time dependence of the spectrum is given by [22]

$$I(t,\xi) = \frac{I_0}{\Delta\omega} e^{-\mu_{\mathrm{el}} L} \frac{\xi}{\tau_0 t} e^{\frac{-(1+q)t}{\tau_0}} J_1^2\left(2\sqrt{\frac{\xi t}{\tau_0}}\right), \tag{2.3.2}$$

where I_0 is the initial intensity in the frequency band $\Delta\omega$ determined by the monochromator, μ_{el} is the electronic absorption length, L is the sample thickness, $J_1(x)$ is the first order Bessel function and $q > 0$ accounts for line broadening such as caused by a distribution of spectral parameters, which leads to a faster decay. As the effective thickness is temperature dependent only through the temperature dependence of the Lamb-Mössbauer factor, measuring the effective thickness as a function of temperature allows one to determine the Lamb-Mössbauer factor.

2.3.2 Nuclear inelastic scattering

Nuclear inelastic scattering is a phonon spectroscopy method based on the Mössbauer effect and gives access to the density of phonon states of Mössbauer isotopes from the nuclear absorption spectrum [23–25]. Detailed overviews of the technique are given for example in Refs. [22, 26].

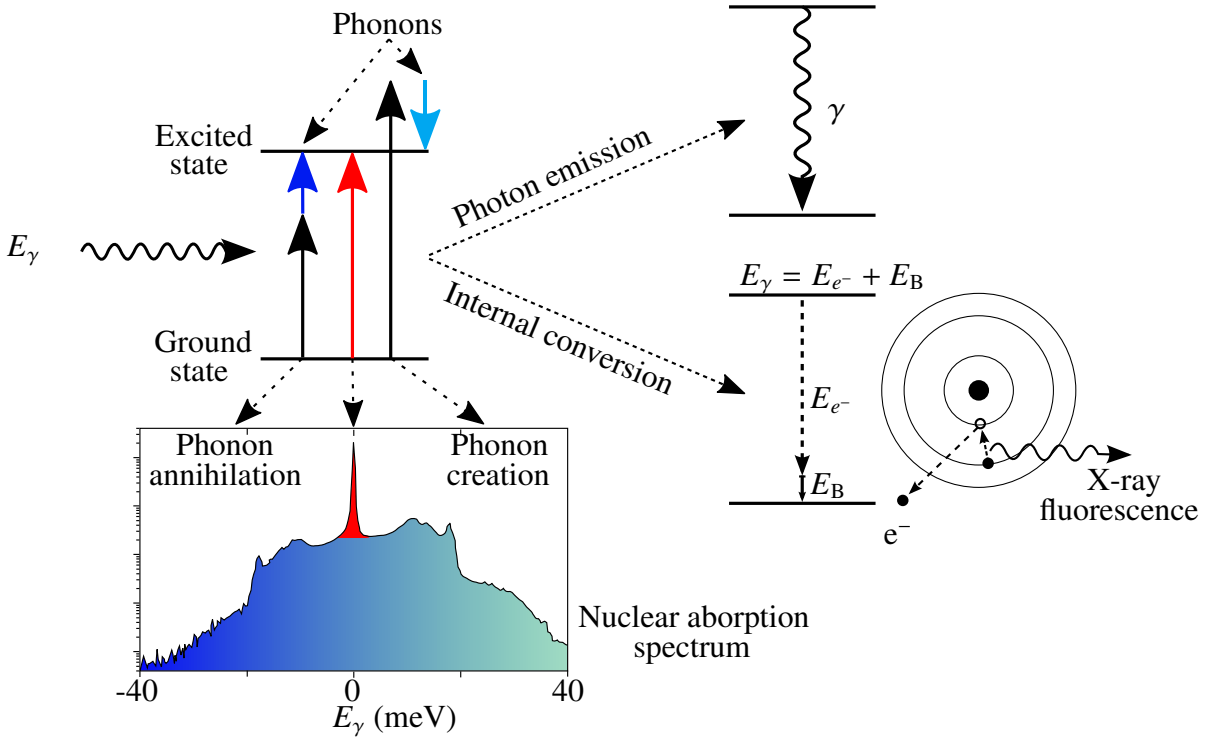

Figure 2.9: Basic principle of nuclear inelastic scattering. Synchrotron radiation tunable in energy is used excite the Mössbauer transition of a nucleus. If the photon energy matches the one of the Mössbauer transition (red arrow) the photon is directly absorbed by the nucleus. If the energies do not match the photon can still be absorbed by the assistance of phonons (blue arrows) thereby creating or annihilating one or more phonons. The excited nucleus subsequently decays either via photon emission or via internal conversion to the ground state. The kinetic energy of the emitted conversion electron, E_{e^-}, is determined by its binding energy, E_B, and the energy of the nuclear transition, E_γ. In the drawing the emission of a conversion electron from the K-shell is shown. The internal conversion is followed by emission of characteristic X-ray fluorescence. The measured nuclear absorption spectrum relative to the energy of the Mössbauer transition consists of an elastic part (red) and an inelastic part (blue) from which the density of phonon states can be obtained.

The basic principle of nuclear inelastic scattering is schematically shown in Figure 2.9. Synchrotron radiation is tuned in energy around the energy of the Mössbauer transition of a Mössbauer active nucleus. At the energy of the Mössbauer transition the photons are directly absorbed in a zero-phonon process. If the photon energy exhibits an excess or deficit with respect to the Mössbauer transition energy only phonon-assisted absorption takes place by creation or annihilation of n phonons, respectively. The zero-phonon process is an elastic process whereas the phonon-assisted process is inelastic. The probability of phonon-assisted absorption at a given energy depends on the number of phonon states available and thus the density of phonon states can be obtained from the nuclear absorption spectrum.
The excited nucleus decays to the ground state via the emission of a photon or via internal conversion and the emission of the concomitant X-ray fluorescence. The delayed X-ray or nuclear fluorescence is an unambiguous indication for the nuclear absorption process to have taken place because there is no other source of radiation. Thus, in a typical experiment one measures the intensity of the fluorescence as a function of the incident photon energy to obtain the nuclear absorption spectrum. A typical nuclear absorption spectrum is shown in Figure 2.9. The peak at zero energy relative to the Mössbauer transition energy originates mostly from the elastic scattering whereas at higher and lower energies the inelastic scattering contribution to the spectrum is observed. The relative fractions of the elastic and inelastic part of the spectrum are given by f_{LM} and $1 - f_{\mathrm{LM}}$, respectively.
In order to correct the nuclear absorption spectrum for the elastic scattering contribution the nuclear forward scattering intensity is simultaneously recorded as a function of energy, because nuclear forward scattering is an elastic process. The resulting instrumental function is subsequently scaled and subtracted from the absorption spectrum. The thus obtained purely inelastic spectrum is expanded in terms of one- and multiphonon processes using a Fourier-Log decomposition [27]. From the one-phonon term the density of phonon states is obtained in a self-consistent way using Lipkin's sum rules which relate the extracted density of phonon states to the inelastic spectrum [28, 29]. The essential steps in the extraction procedure of the density of phonon states are shown in Figure 2.10.
From the nuclear absorption spectrum the temperature, T, of the sample can be determined as the occupation of phonon states is temperature dependent. The probability for nuclear absorption assisted by phonon annihilation (negative energies) is proportional to $n_{\mathrm{B}} = 1/(\exp(|E|/k_{\mathrm{B}}T) - 1)$ and the probability for nuclear absorption assisted by phonon creation (positive energies) is proportional to $(n_{\mathrm{B}} + 1)$ [26]. Thus, from the intensity ratio for phonon creation and annihilation at a given energy $|E|$ the temperature can be determined.

2.4 Inelastic X-ray scattering

A comprehensive overview of inelastic X-ray scattering can be found in Ref. [30, 31]. Inelastic X-ray scattering is a momentum and energy resolved technique giving access to the phonon dispersion by measuring the dynamic structure factor, which is the space and time Fourier transform of the density-density correlation function.
The inelastic scattering process is depicted schematically in Figure 2.11. The incident X-ray beam with well defined energy, E_{i}, and wave vector, $\vec{k}_{\mathrm{i}}$, is scattered at an angle 2θ. The scattered X-ray is defined by the new energy, E_{f}, and wave vector, $\vec{k}_{\mathrm{f}}$. Due to energy and momentum conservation

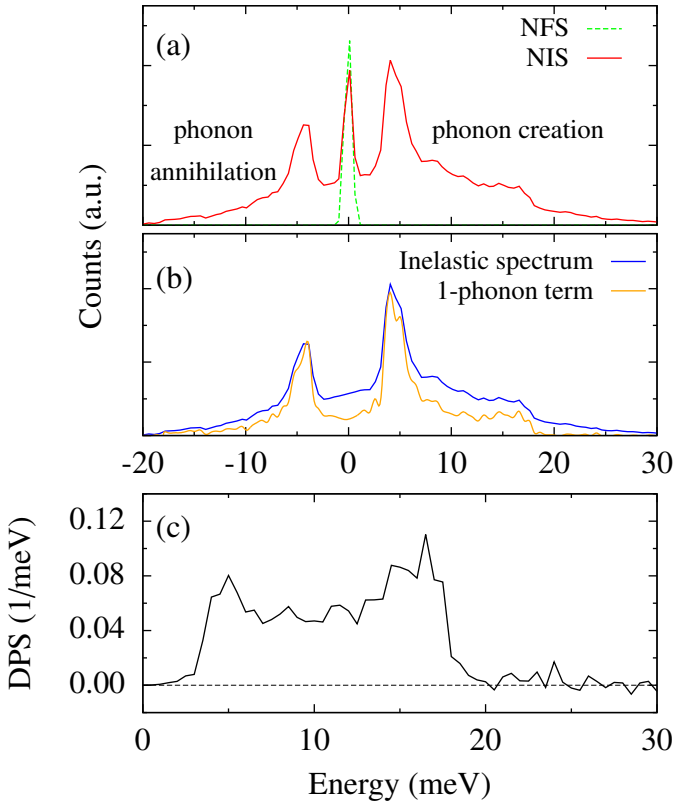

Figure 2.10: Essential steps of the extraction procedure of the density of phonon states (DPS). The data shown here is ^{119}Sn nuclear inelastic scattering by an enriched β-Sn sample at 115 K measured at PETRA III, P01, DESY. (a) Raw nuclear absorption spectrum (NIS) and instrumental function (NFS). The zero energy corresponds to the energy of the Mössbauer transition and positive and negative energies to phonon creation and annihilation, respectively. (b) Inelastic absorption spectrum obtained by scaling and subtracting the instrumental function from the raw nuclear absorption spectrum and the 1-phonon term obtained through a Fourier-Log decomposition of the inelastic spectrum in terms of n-phonon processes. (c) Density of phonon states obtained from the 1-phonon term.

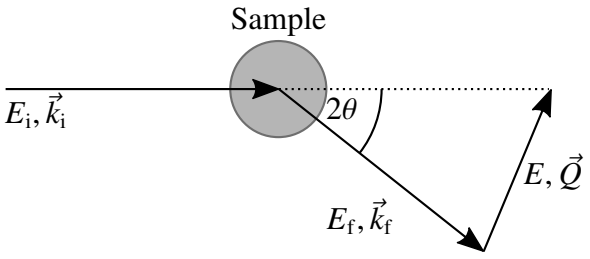

Figure 2.11: The inelastic scattering process. $E_{\mathrm{i,f}}$ and $\vec{k}_{\mathrm{i,f}}$ are energy and wave vector of the incident and scattered X-ray, respectively. 2θ is the scattering angle. E and $\vec{Q}$ are energy and momentum transfer.

it follows that:

$$\vec{Q} = \vec{k}_\mathrm{i} - \vec{k}_\mathrm{f} \tag{2.4.1}$$

$$E = E_\mathrm{i} - E_\mathrm{f} \tag{2.4.2}$$

$$Q^2 = k_\mathrm{i}^2 + k_\mathrm{f}^2 - 2k_\mathrm{i}k_\mathrm{f}\cos(2\theta). \tag{2.4.3}$$

Assuming for the energy transfer $E \ll E_\mathrm{i}$, as the energy of a phonon is much smaller than the X-ray energy, the magnitude of the momentum transfer, Q, is given by the magnitude of the wave vector of the incoming X-ray and the scattering angle

$$Q = 2k_\mathrm{i}\sin(\theta). \tag{2.4.4}$$

As demonstrated very recently in Ref. [32], inelastic X-ray scattering from powder samples can be utilized to determine the generalized density of phonon states by averaging the inelastic X-ray scattering spectrum over a large Q sphere. The generalized density of phonon states is the sum of the normalized partial densities of phonon states per element weighted by the scattering power of each element in the measured Q range. Therefore, the generalized density of phonon states is a distorted version of the real density of phonon states. The extraction procedure of the generalized density of phonon states is similar to the one for nuclear inelastic scattering described above.
A typical experimental setup for inelastic X-ray scattering as used at beam line ID28 at the European Synchrotron Radiation Facility is shown schematically in Figure 2.12. The X-ray radiation is monochromatized using a silicon backscattering monochromator operated at a backscattering angle of 89.98 °. The energy of the backscattered radiation depends on the chosen Si(n n n) reflection and is tuned by changing the temperature of the monochromator with mK precision. The radiation scattered from the sample is analysed in energy by crystal analysers operated in backscattering geometry utilizing the same Si(n n n) reflection as the monochromator, however, the crystal analyser is kept at constant temperature. The inelastic scattering spectrum is then recorded as a function of the difference in energy determined by the monochromator and analyser temperatures. The momentum transfer Q is determined by the chosen scattering angle. At ID28 the spectrometer is equipped with nine crystal analysers allowing to record nine spectra at different momentum transfers simultaneously.

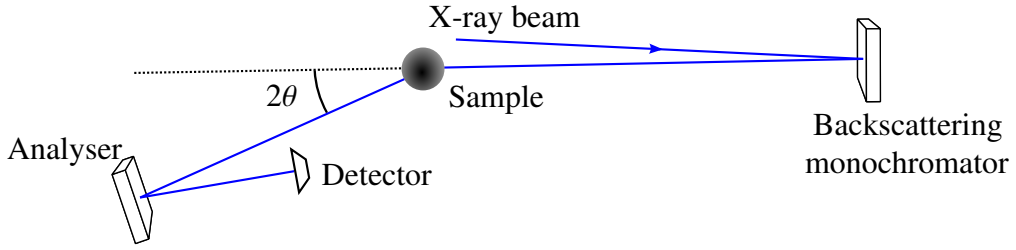

Figure 2.12: Schematic experimental setup for inelastic X-ray scattering as used at beam line ID28 at the European Synchrotron Radiation Facility. The momentum transfer is defined by the scattering angle 2θ.

Chapter 3

3

Nuclear forward scattering by the 68.7 keV state of ^{73}Ge in $CaGeO_3$ and GeO_2

Abstract

We measured nuclear forward scattering of synchrotron radiation by the 68.7 keV nuclear resonance of ^{73}Ge with a half life of $T_{\frac{1}{2}} = 1.74$ ns. The Debye temperatures of $CaGeO_3$ in the wollastonite, garnet and perovskite phases were determined to be 386(20) K, 437(20) K and 507(20) K, respectively, and 309(20) K and 459(11) K for GeO_2 in the quartz and rutile phases, respectively. The isomer shift is clearly dependent on the Ge valence but not directly on the coordination geometry. The so far unknown magnetic moment μ_e of the 68.7 keV excited state of ^{73}Ge is determined to be $-0.84(22)\,\mu_N$. Time domain ^{73}Ge Mössbauer spectroscopy with the 68.7 keV resonance is feasible for isomer shift and Debye temperature measurements but so far no electric quadrupole nor magnetic hyperfine interactions could be observed.

R. E. Simon[1,2], I. Sergueev[1,3], J. Perßon[1], C. A. McCammon[4], F. Hatert[5] and R. P. Hermann[1,2]

[1] *Jülich Centre for Neutron Science JCNS and Peter Grünberg Institut PGI, JARA-FIT, Forschungszentrum Jülich GmbH, D-52425 Jülich, Germany*

[2] *Faculté des Sciences, Université de Liège - B-4000 Liège, Belgium*

[3] *Deutsches Elektronen-Synchrotron - D-22607 Hamburg, Germany*

[4] *Bayerisches Geoinstitut, Universität Bayreuth, D-95440 Bayreuth, Germany*

[5] *Laboratoire de Minéralogie, Université de Liège - B-4000 Liège, Belgium*

3.1 Introduction

Two excited nuclear states of the ^{73}Ge isotope at 13.2845(15) and 68.752(7) keV with half lives of $T_{\frac{1}{2}} = 2.92(3)\,\mu$s and $T_{\frac{1}{2}} = 1.74(13)$ ns, respectively [33], are suitable for Mössbauer spectroscopy. The first observation of the Mössbauer effect on the 68.7 keV state by Czjzek *et al.* [34] dates back to 1966. Coulomb excitation was used to populate the excited state. Czjzek *et al.* [35] and Zimmermann *et al.* [36] conducted the first Mössbauer experiments on the 68.7 keV state in Ge and GeO_2 in the rutile and quartz phases in 1968. In 1974, Raghavan and Pfeiffer [37] were the first to observe the Mössbauer effect on the 13.3 keV state of ^{73}Ge with a ^{73}As source. Ge Mössbauer spectroscopy (MS) is undoubtedly a valuable technique to study the chemistry and physics of Ge in a variety of material systems, *e.g.* in Ge bearing semiconductor devices for the investigation of defects [38] or in phase change materials where the Ge coordination is still a matter of debate [39, 40]. The applicability of ^{73}Ge MS to the study of solid state physics is, however, limited due to severe experimental difficulties [35–37, 41]. For the 68.7 keV transition a Coulomb excited source is necessary and the 13.3 keV transition exhibits a high internal conversion factor and large electronic absorption cross section due to absorption K-edge absorption at 11.1 keV in close proximity to the transition energy resulting in a small cross section for the γ-rays. Alternatively, synchrotron radiation can be used to populate the excited states of Mössbauer isotopes. Recently, Seto *et al.* applied synchrotron radiation-based MS to the 68.7 keV state of ^{73}Ge using GeO_2 quartz (96.4 % ^{73}Ge enriched) as a reference absorber to record an energy domain spectrum of Li_2GeO_3 (natural ^{73}Ge abundance) with a total acquisition time of $\sim$ 90 h [42].
Here we report on the application of nuclear forward scattering (NFS) [43] to the ^{73}Ge 68.7 keV Mössbauer transition. The experimental setup includes a $\sim$ 24 meV energy bandwidth monochromator and a multielement detector. We investigated two model systems, $CaGeO_3$ and GeO_2, with distinct structural environments of tetravalent Ge in four-, mixed four/six- and six-fold Ge coordination. In addition, we studied GeS and GeSe with divalent Ge and pure Ge. These samples are ideal to study the influence of chemical bonding on the isomer shift. The lattice dynamics were studied by the determination of the Lamb-Mössbauer factor and the Debye temperature. The GeO_2 measurements allowed us to validate the results obtained by MS [35], [36]. We performed measurements with an applied magnetic field in order to determine the so far unknown nuclear magnetic moment μ_e of the ^{73}Ge excited state.

3.2 Experimental setup

The experiment was performed at the nuclear resonance beamline ID18 at the European Synchrotron Radiation Facility. The storage ring was operated in the 16 bunch filling mode with a time window of 176 ns and an average beam current of 70 mA. The 68.7 keV incident radiation was monochromatized in two steps by a high-heat-load monochromator with Si (111) reflections followed by a medium-resolution monochromator composed of two pairs of Si (444) and Si (844) reflections arranged in a nested configuration [43]. The optical design of the reflections is similar to the one in Ref. [44, 45]. In order to improve the throughput of the monochromators the radiation was collimated by compound refractive lenses installed before the high-heat-load monochromator. The instrumental function, measured with $^{73}GeO_2$ rutile, has pseudo-Voigt shape with an energy

bandwidth of 24(1) meV FWHM (Figure 3.1). The radiation scattered by the sample in forward direction was measured using a 16-element array of Si avalanche photodiodes which allows the separation in time of the electronic scattering from the nuclear resonant scattering and has ~ 10 % efficiency, less than 0.02 Hz electronic noise and ~ 0.5 ns time resolution. The acquisition time per spectrum was ~ 1 – 2 h. The samples were placed in a cryomagnetic system with 3 K base temperature.

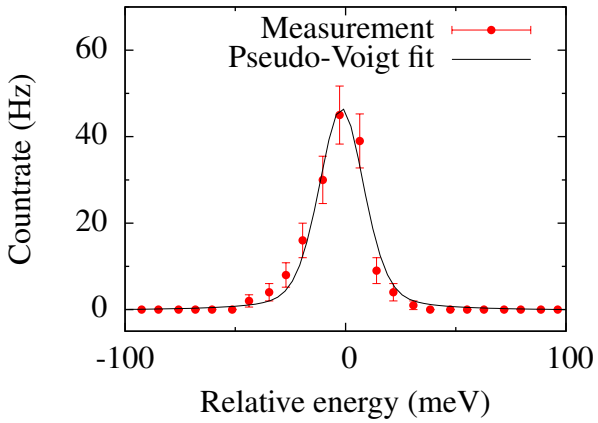

Figure 3.1: The instrumental function, measured with $^{73}GeO_2$ rutile. The line represents a fit with a pseudo-Voigt function with 24(1) meV FWHM.

3.3 Sample preparation

All investigated samples except the two GeO_2 samples and Ge have natural isotopic abundance of 7.73 % ^{73}Ge. $CaGeO_3$ wollastonite was synthesized by calcinating a stochiometric mixture of $CaCO_3$ and GeO_2 (quartz) at a temperature of 1200 °C for 6 h. The garnet phase of $CaGeO_3$ was synthesized from the wollastonite phase in a piston cylinder press at 1000 °C and a pressure of 3 GPa for 2 h. The $CaGeO_3$ garnet was then used as starting material for the synthesis of the $CaGeO_3$ perovskite which was conducted in a multianvil press at 1100 °C and 10 GPa for 2 h. Enriched $^{73}GeO_2$ in the rutile phase was hydrothermally synthesized from quartz-type $^{73}GeO_2$, 95.6 % ^{73}Ge enriched, at 600 °C and 0.1 GPa for 7 days. GeS powder was purchased from Sigma Aldrich. GeSe was synthesized from a stochiometric mixture of Ge and Se in Ar atmosphere at 1000 °C for 7 h. Ge, 95.6 % ^{73}Ge enriched, was purchased from Chemgas. All samples were polycrystalline and phase purity was confirmed by x-ray powder diffraction.

3.4 Experimental method

The time dependent NFS signal is determined by hyperfine interactions, multiple scattering effects and the nuclear spins of the ground and excited state. The 68.7 keV state of ^{73}Ge has a nuclear spin of $I_e = 7/2$ and the ground state a spin of $I_g = 9/2$. The hyperfine interactions lift the degeneracy

of the ground and excited nuclear states. This causes a periodic modulation of the NFS signal with frequencies proportional to the strength of the hyperfine interaction. Multiple scattering within the sample also leads to a time modulation with a frequency dependent on the thickness of the sample L, the Lamb-Mössbauer factor f_{LM} and the life time τ_0 of the excited state. f_{LM} is the recoil-free emission and absorption probability of γ-radiation by a nucleus. All NFS spectra of single compounds measured herein can be described solely by multiple scattering through a single line absorber, *i.e.* without measurable hyperfine splitting. The time dependence of the spectra is then simply given by [22]

$$I(t,\xi) = \frac{I_0}{\Delta\omega} e^{-\mu_{\mathrm{el}} L} \frac{\xi}{\tau_0 t} e^{\frac{-(1+q)t}{\tau_0}} J_1^2\left(2\sqrt{\frac{\xi t}{\tau_0}}\right), \tag{3.4.1}$$

where I_0 is the initial intensity in the frequency band $\Delta\omega$ determined by the monochromator, μ_{el} is the electronic absorption length, L is the sample thickness, $J_1(x)$ is the first order Bessel function, $q > 0$ accounts for line broadening such as caused by a distribution of spectral parameters, which leads to a faster decay, and ξ is the effective thickness

$$\xi = \frac{1}{4} L \frac{\beta}{V_{\mathrm{Ge}}} \sigma_0 f_{\mathrm{LM}}. \tag{3.4.2}$$

β is the isotopic enrichment factor, V_{Ge} is the volume per Ge atom and σ_0 is the nuclear resonant absorption cross section. In order to account for inhomogenities in the sample thickness a distribution with five supporting points was used. The multiple scattering is nicely demonstrated in the case of GeO_2 rutile (Figure 3.2). The exponential decay due to the life time of the excited state is modulated by dynamical beats. With increasing temperature the beating period increases due to the decrease of f_{LM} (see Figure 3.3) and the beats are smeared out due to thickness imhomogenities within the sample. We use a Levenberg-Marquardt algorithm to fit Eq. 3.4.1 to the NFS spectra. In addition, we use the MOTIF code [46] for the analysis of magnetic hyperfine interactions and isomer shifts.

3.5 Results and discussion

3.5.1 Samples and spectra

We measured the NFS signal in $CaGeO_3$ garnet, perovskite and wollastonite, in $^{73}GeO_2$ quartz and rutile and in ^{73}Ge between $\sim$ 60 and 298 K. These compounds exhibit different coordination numbers for Ge, are non-magnetic and in case of GeO_2 show an electric field gradient on the Ge site as determined by NMR [47]. Ge crystallizes in the space group $Fd\bar{3}m$ with one Ge site that has cubic symmetry. The Mössbauer spectrum of Ge at 80 K does not show any hyperfine interactions and can be described as a single line absorber [36]. We therefore expect the NFS spectrum to exhibit only dynamical scattering according to Eq. 3.4.1. GeO_2 quartz crystallizes in the trigonal crystal system with Ge tetrahedrally coordinated by O. The Ge nuclei on this site are subject to an electric field gradient (EFG) resulting in a quadrupolar coupling constant $C_{\mathrm{Q}} = 9.2(5)$ MHz [47]. GeO_2 rutile adopts the tetragonal crystal structure with Ge six-fold coordinated by a distorted O octahedron. ^{73}Ge solid-state NMR revealed a quadrupolar coupling constant $C_{\mathrm{Q}} = 19.3(5)$ MHz

[47]. MS, however, revealed no observable hyperfine interactions and single line spectra [35, 36] for both GeO_2 phases. We thus expect the NFS spectra of both phases to obey Eq. 3.4.1 with a possible line broadening $q > 0$ due to the EFG which should be larger for the rutile than the quartz phase. The Lamb-Mössbauer factor and Debye temperature should also be larger than for the quartz phase because the high-pressure rutile phase exhibits a smaller V_{Ge} and a more rigid lattice. In the triclinic $CaGeO_3$ wollastonite Ge is tetrahedrally coordinated by O. The hyperfine parameters of ^{73}Ge in this compound are so far unknown. We attempt to describe the NFS spectrum by Eq. 3.4.1 with a possible line broadening q. $CaGeO_3$ garnet adopts a tetragonal crystal structure where Ge occupies four- and six-fold O coordinated sites. Thus, we expected the NFS spectra to consist of two absorption lines, either separated by a measurable isomer shift or described as one broad line with a value of $q > 0$. In orthorhombic $CaGeO_3$ perovskite Ge is six-fold coordinated by an O octahedron and we describe the NFS spectra similar to those of wollastonite. The Lamb-Mössbauer factor and Debye temperature of the wollastonite phase are expected to be lowest of the three because it is the ambient pressure phase and exhibits the largest V_{Ge}, whereas they should be the highest for the high-pressure perovskite phase due to the smallest V_{Ge}. The NFS spectra and fits are shown in Figure 3.2.
Although there is an electric field gradient present at the Ge site in GeO_2 quartz and rutile [47] no hyperfine interactions are observable, in line with MS results [35, 36]. This can be related to a small nuclear quadrupole moment of the excited state. However, quadrupole hyperfine interactions might be observed in compounds with larger electric field gradients, *e.g.* Ge-V layered compounds [48]. The $CaGeO_3$ garnet NFS spectra reveal also a single line absorber which indicates that the difference in the Ge coordination between the two sites does not cause a measurable splitting of the absorption lines.

3.5.2 Lattice dynamics

In the Debye approximation, the Lamb-Mössbauer factor f_{LM} is a function of the temperature T and the Debye temperature Θ_D, see ref. [14]. As $\xi(T)$ is directly proportional to $f_{LM}(T)$, see Eq. 3.4.2, $f_{LM}(T)$ and Θ_D are obtained by separating $\xi(T)$ into a temperature independent and sample dependent fit parameter $L\beta\sigma_0/(4V_{Ge})$ and the temperature dependent $f_{LM}(T)$. Two data points are sufficient in the Debye approximation in order to determine these two fit parameters and thus Θ_D. We estimate the uncertainty to $\Delta\Theta_D = \pm 20\,K$. With more than two data points the uncertainties can be directly obtained from the fit procedure. The results are shown in Figure 3.3 and Table 3.1 together with MS results [35, 36]. Among the $CaGeO_3$ phases the perovskite exhibits the highest Θ_D whereas wollastonite exhibits the lowest, and this matches our expectations. The same relation is observed for the high-pressure rutile phase of GeO_2 which reveals a higher Θ_D than the quartz phase. f_{LM} can also be estimated from mean square displacements $\langle u^2 \rangle$ according to $f_{LM} = \exp(-k_\gamma^2 \langle u^2 \rangle)$ with the wave vector $k_\gamma = 34.9\,Å^{-1}$ using published XRD data [49–53] at room temperature, see Figure 3.3. The calculated values of f_{LM} at 78 K according to the Debye approximation agree well with the literature data for GeO_2 quartz and rutile [35, 36]. The values obtained from room temperature XRD data are also in good agreement with our results. For Ge, however, our results deviate strongly from ref. [36], but agree with ref. [54]. The XRD data for the $CaGeO_3$ polymorphs give lower values for f_{LM} than the NFS measurements. These deviations are probably related to an overestimated $\langle u^2 \rangle$ in the refinement of the XRD data. With these high values of f_{LM} ^{73}Ge nuclear resonance scattering can be extended to nuclear inelastic scattering (NIS)

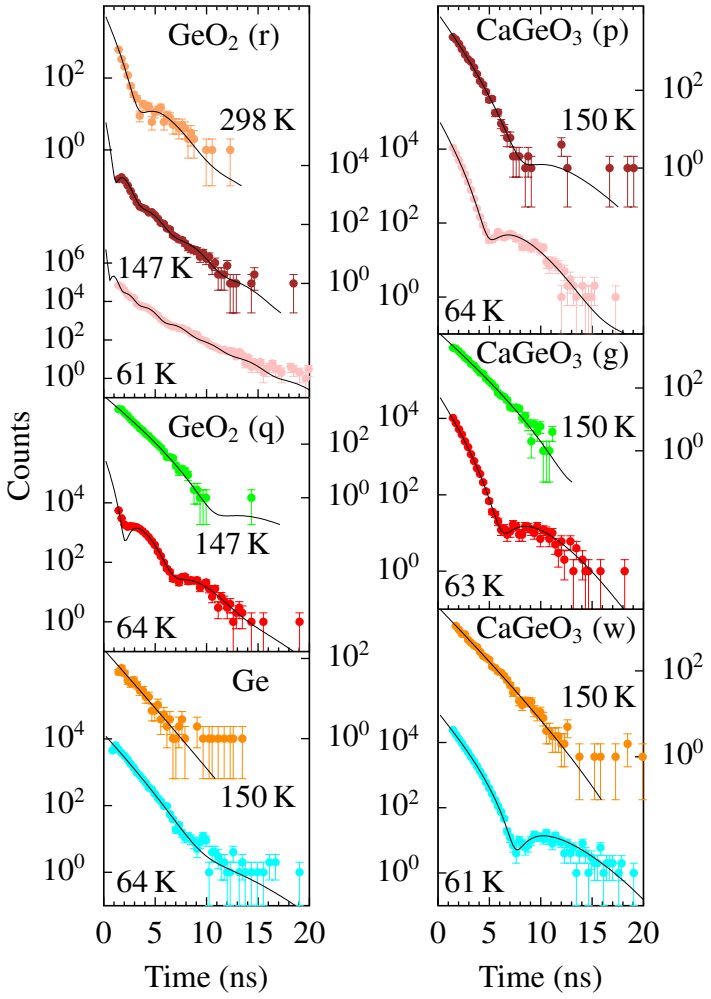

Figure 3.2: The NFS spectra of $^{73}GeO_2$ quartz and rutile, $CaGeO_3$ wollastonite, garnet and perovskite and pure ^{73}Ge between ~ 60 and ~ 298 K. The lines are the fit to the data.

	θ_D(K)	
	This work	Ref. [36, 54]
$CaGeO_3$ (w)	386(20)	
$CaGeO_3$ (g)	437(20)	
$CaGeO_3$ (p)	507(20)	
$^{73}GeO_2$ (q)	309(20)	255(16)
$^{73}GeO_2$ (r)	459(11)	426(16)
^{73}Ge	399(20)	263(11), 374(2)

Table 3.1: The Debye temperatures θ_D obtained from the fit of the effective thickness $\xi(T)$.

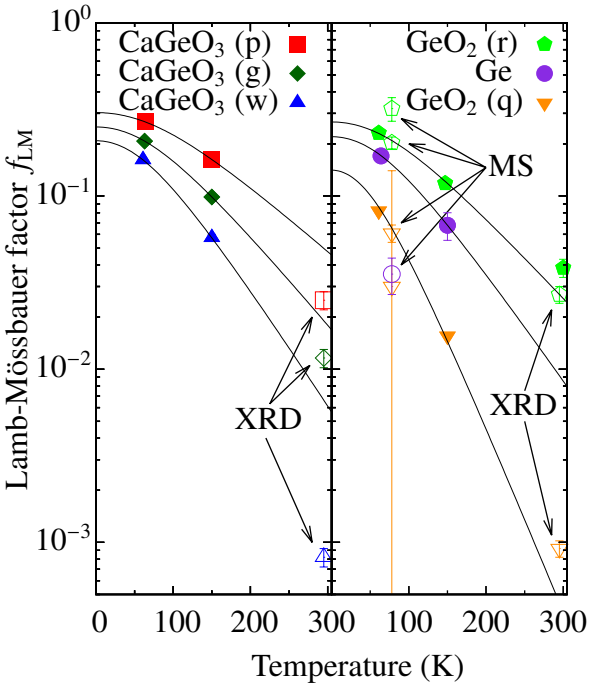

Figure 3.3: $f_{\mathrm{LM}}(T)$ (filled symbols) in $CaGeO_3$ garnet, perovskite and wollastonite, $^{73}GeO_2$ quartz and rutile and ^{73}Ge obtained from the effective thickness $\xi(T)$. The lines are the fits according to the Debye approximation [14]. Open symbols correspond to Mössbauer spectroscopy (MS) results [35, 36] and XRD results [49–53].

for measurements of the density of phonon states (DPS) provided that a meV energy resolution monochromator can be designed, *e.g.* by using a sapphire backscattering monochromator [55].

3.5.3 Nuclear magnetic moment of the excited state

The nuclear magnetic moment μ_e of the 68.7 keV excited state of ^{73}Ge is unknown. In order to put a constraint on its value the NFS was measured for diamagnetic $CaGeO_3$ in the wollastonite phase at 150 K in an applied magnetic field of 0 and 5 T, see Figure 3.4. The time spectra are essentially identical which indicates that the magnetic moment of the excited and ground state must be similar. We can fit both spectra simultaneously according to Eq. 3.4.1 with one set of parameters, which yields $\xi = 0.41(4)$ without taking any hyperfine interactions into account. As no hyperfine splitting is visible a range can be determined for μ_e. We fitted the time spectrum for different values of μ_e under the assumption of randomly oriented nuclear spins in a magnetic field of 5 T. The nuclear magnetic moment of the ground state is $\mu_g = -0.878241(44)\,\mu_{\mathrm{N}}$ [56]. The only free fit parameter is then a scaling factor. The best fit is obtained for $\mu_e = -0.84\,\mu_{\mathrm{N}}$ with $\chi^2 = 43.6$ (Figure 3.4) and the number of degress of freedom, $n = 37$. At a 95 % confidence μ_e must lie in the range $-1.06\,\mu_{\mathrm{N}} \leq \mu_e \leq -0.62\,\mu_{\mathrm{N}}$. Larger hyperfine fields at the Ge nucleus might, however, be found in Fe-Ge alloys [57] or $ErGe_3$ [58].

3.5.4 Isomer shifts

In contrast to MS the determination of the isomer shift, δ, with NFS requires an additional second absorber as a reference compound. The NFS of a mixture of two compounds with different

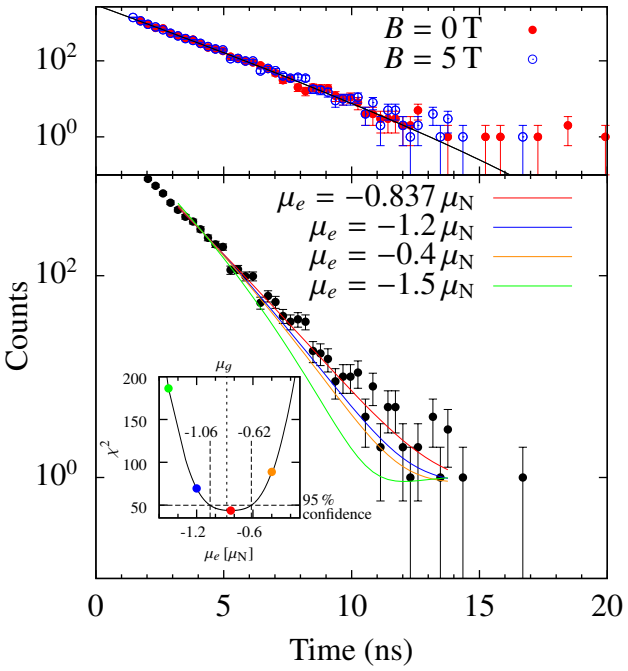

Figure 3.4: Top: NFS for $CaGeO_3$ wollastonite at 150 K with and without an applied magnetic field of 5 T. Lines are the fits to the data, with Eq. 3.4.1 and $\xi = 0.41(4)$. The two fits are not distinguishable. Bottom: NFS measured in $CaGeO_3$ wollastonite at 5 T and 150 K. The lines are modelled with different nuclear magnetic moments μ_e of the excited state. Inset: The goodness of the fit criterion χ^2 as a function of the nuclear magnetic moment μ_e of the excited state.

δ exhibits beats which arise from the interference of the corresponding absorption lines with a frequency dependent on the relative isomer shift [22]. The NFS time spectra of GeS and GeSe (Figure 3.5) both can be described through single line absorbers according to Eq. 3.4.1 and are consequently suitable reference compounds. In order to determine δ of $CaGeO_3$, in wollastonite, garnet and perovskite, and GeO_2, in quartz and rutile modifications, we measured the NFS of mixtures of those compounds with GeS and GeSe between 3 and 298 K (Figure 3.5). For the fit of the time spectra we calculated f_{LM} of the compound under investigation from the obtained Debye temperature. f_{LM} of the reference compound - GeS or GeSe - and δ are free fit parameters. The results are shown in Figure 3.5 and Table 3.2. δ of quartz and rutile GeO_2 vs. GeS measured at 98 and 298 K, respectively, were corrected to 15 K for the second order Doppler shift (SOD) [59] using the obtained Debye temperatures. NFS is sensitive to the modulus of δ. According to the weighted average of [35, 36], the MS isomer shifts of GeO_2 quartz and rutile with respect to Ge are $-1.00(8)$ and $-0.88(8)$ mm/s, respectively. We assume that δ^{GeS} of both GeO_2 phases with respect to GeS have the same sign. δ^{GeS} of quartz must be smaller than δ^{GeS} of rutile which indicates that our measured values for GeO_2 must have a negative sign and we can calculate $\delta^{GeS} = -0.67(8)\,\Gamma_0$ for Ge, where we corrected for the SOD to 15 K and used the conversion factor $1\,\Gamma_0 = 1.14(9)$ mm/s. We obtain $\delta = 0.32(9)\,\Gamma_0$ between GeO_2 quartz and rutile which is in agreement with [35, 36]. ^{119}Sn MS shows the same order of δ for SnO_2, α-Sn and SnS [60–62]. In analogy to ^{119}Sn MS

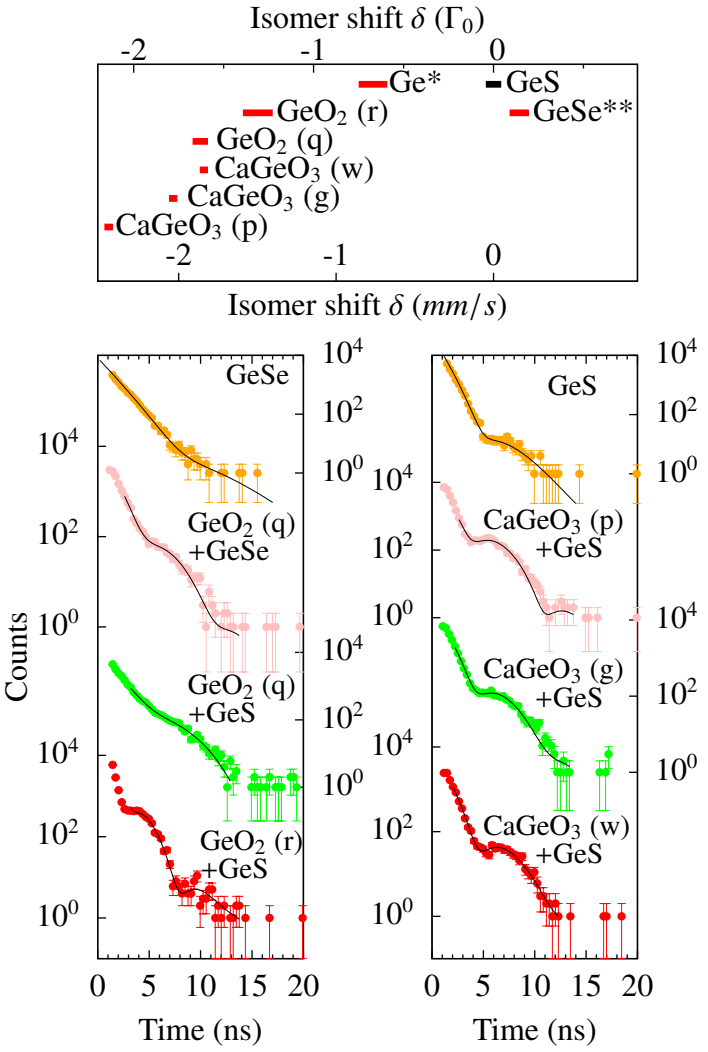

Figure 3.5: Left: The NFS of mixtures of $^{73}GeO_2$ quartz and rutile with GeS at 98 and 298 K, respectively, of $^{73}GeO_2$ quartz and GeSe at 15 K and of pure GeS and GeSe at 3 K. Right: The NFS of mixtures of the $CaGeO_3$ phases with GeS at 15 K. Lines are the fit to the data. Top: The isomer shifts with respect to GeS at 15 K. *Ge was calculated from our results and [35], [36]; **GeSe from the GeO_2 vs. GeSe measurement.

of $CaSnO_3$ we assume δ^{GeS} of the $CaGeO_3$ polymorphs to be negative [61]. Our measured δ^{GeSe} of GeO_2 quartz with respect to GeSe, $\delta^{GeSe} = -1.77(3)\,\Gamma_0$, must be negative [36] and is in good agreement with $\delta = -2.05(46)\,\Gamma_0$ in ref. [36]. Thus, for GeSe $\delta^{GeS} = 0.14(5)\,\Gamma_0$.
The isomer shift is a function of the electron density at the nucleus and accordingly the valence of Ge. In the GeO_2 and $CaGeO_3$ modifications ionic bonding of Ge(IV) is predominant. In GeS and GeSe, the Ge is divalent. As seen from Figure 3.5, values for Ge(II) and Ge(IV) compounds cluster together, which justifies our assumption of a negative isomer shift of the $CaGeO_3$ polymorphs with respect to GeS. The isomer shift is also a function of the structural environment. $CaGeO_3$ in wollastonite and GeO_2 in the quartz modification exhibit the same isomer shift. This is in line with the same Ge-O bond length in $CaGeO_3$ wollastonite and GeO_2 quartz [63, 64] and with the

common four-fold Ge coordination. The structural environment in these two compounds as seen by Ge K-edge EXAFS is also very similar [63]. In contrast, in $CaGeO_3$ perovskite and GeO_2 rutile we find significantly different isomer shifts despite the similar six-fold Ge coordination, a difference ascribed to the location of Ge in GeO_2 rutile in a distorted octahedron with four short and two long Ge-O bonds [64] whereas there are six Ge-O bonds of similar length in $CaGeO_3$ perovskite [49, 65]. In $CaGeO_3$ garnet the Ge occupies two distinct crystallographic sites with a four- and six-fold coordination. We determined the isomer shift under the assumption of a single nuclear site because the NFS is consistent with a single line absorber (Figure 3.2). Thus clearly, δ is not governed unambiguously by the Ge coordination geometry. Considering the different Ge-O bond lengths and the volumes of the O octa- and tetrahedra surrounding the Ge we find no evidence for a correlation between the structure and δ. The separation of $CaGeO_3$ and GeO_2 in δ indicates a significant influence of the presence of other cations, Ca(II), on δ.

	$\delta(\Gamma_0)$	reference
$^{73}GeO_2$ rutile	-1.31(8)	GeS
$^{73}GeO_2$ quartz	-1.63(4)	
$CaGeO_3$ wollastonite	-1.61(2)	
$CaGeO_3$ garnet	-1.78(2)	
$CaGeO_3$ perovskite	-2.14(2)	
Ge*	-0.67(8)	
$^{73}GeO_2$ quartz	-1.77(3)	GeSe

Table 3.2: Isomer shifts δ of $CaGeO_3$ and $^{73}GeO_2$ with respect to GeS and GeSe in units of the natural line width $\Gamma_0 = 1.14(9)$ mm/s at 15 K; *calculated from [35], [36] and our results. δ of GeO_2 quartz and rutile and Ge were corrected for the second order Doppler shift to 15 K.

3.6 Conclusion

Nuclear forward scattering by the third excited nuclear state of ^{73}Ge with an energy of 68.7 keV was measured in a series of compounds and Lamb-Mössbauer factors and the Debye temperatures of Ge in $CaGeO_3$ garnet, perovskite and wollastonite, ^{73}Ge and $^{73}GeO_2$ quartz and rutile were determined. Our results agree with the literature for Ge and GeO_2 quartz and rutile. Measurements of the isomer shift relative to GeS and GeSe revealed a clear dependence of the isomer shift on the Ge valence but no direct dependence of the isomer shift on the Ge coordination geometry. Neither quadrupole nor magnetic hyperfine interactions have been observed. The so far unknown magnetic moment μ_e of the excited state of ^{73}Ge is determined to be $\mu_e = -0.84(22)\,\mu_N$. Compared to conventional and synchrotron-radiation-based MS ^{73}Ge NFS is a faster experimental technique which can be easily applied even to samples with natural abundance of ^{73}Ge.

3.7 Acknowledgments

The authors acknowledge the European synchrotron radiation facility for provision of beam time at ID18, R. Rüffer and F. Lange for support during the experiment, financial support by the Deutsche Forschungsgemeinschaft within the SFB917 'Nanoswitches' and G. Manthilake for performing the $CaGeO_3$ perovskite synthesis.

Chapter 4

4

^{121}Sb and ^{125}Te nuclear inelastic scattering in Sb_2Te_3 under high pressure

Abstract

We investigated the lattice dynamics of Sb_2Te_3 under high pressure using ^{121}Sb and ^{125}Te nuclear inelastic scattering of synchrotron radiation. We measured the room temperature ^{121}Sb and ^{125}Te inelastic spectra at 15(1) GPa and 77(3) GPa and extracted the Te and Sb element specific density of phonon states of δ-Sb_2Te_3 at 77(3) GPa. X-ray diffraction confirms the sample to be in the cubic δ-Sb_2Te_3 phase with space group $Im\bar{3}m$ and lattice constant $a = 3.268(4)$ Å. The total density of phonon states of δ-Sb_2Te_3 strongly resembles the one of amorphous $GeSb_2Te_4$, suggesting the presence of covalent bonding in contrast to the resonance bonding in α-Sb_2Te_3. From the density of phonon states of δ-Sb_2Te_3 a mean speed of sound of 2.61(6) km/s and Debye temperatures of 278(10) K for Te and 296(10) K for Sb were determined.

R. E. Simon[1,2], I. Sergueev[3], I. Kantor[4], A. Kantor[4], J. Perßon[1] and R. P. Hermann[1,2]

[1] *Jülich Centre for Neutron Science JCNS and Peter Grünberg Institut PGI, JARA-FIT, Forschungszentrum Jülich GmbH, D-52425 Jülich, Germany*

[2] *Faculté des Sciences, Université de Liège - B-4000 Liège, Belgium*

[3] *Deutsches Elektronen-Synchrotron - D-22607 Hamburg, Germany*

[4] *European Synchrotron Radiation Facility, BP 220, F-38043 Grenoble, France*

4.1 Introduction

Sb_2Te_3 and related Pn_2X_3 (Pn=Bi, Sb; X=S, Se, Te) compounds have attracted much interest in recent years due to their applications in various fields. They are widely known for their high thermoelectric efficiency especially close to room temperature [66]. More recently, Sb_2Te_3 was found to be a topological insulator [67]. $(Sb_2Te_3)_m$-$(GeTe)_n$ ternary compounds are further utilized as phase change materials for optical data storage products and are among the most promising candidates for non-volatile memory devices [2].
The applicability of Sb_2Te_3 as a thermoelectric and phase change material is, among other properties, enabled by its rather low thermal conductivity [2, 66]. The thermoelectric efficiency is characterized by the figure of merit, $ZT = \sigma S^2 T/\kappa$, with the Seebeck coefficient, S, the electrical conductivity, σ, and the thermal conductivity, κ. The thermal conductivity consists of an electronic and a lattice contribution. For the design of new thermoelectric devices with high efficiencies a detailed knowledge of the lattice dynamics is essential. High pressure investigations provide much information about the microscopic lattice dynamics as the materials properties can be finely tuned while the inter-atomic distances are reduced. In particular, the Grüneisen parameter which characterizes the degree of anharmonicity is important as it determines the phonon mean life time and thus the lattice thermal conductivity [68].
Several high pressure studies on Sb_2Te_3 have revealed three phase transitions from ambient pressure up to 53 GPa [69–72]. At ambient pressure Sb_2Te_3 adopts a rhombohedral structure, α-Sb_2Te_3, with space group $R\bar{3}m$. At $\sim$ 8 GPa a new phase, β-Sb_2Te_3, with space group *C2/m* evolves which transforms into another monoclinic structure, γ-Sb_2Te_3, with space group *C2/c* at $\sim$ 13 GPa. At $\sim$ 30 GPa, a transition into a disordered body-centred cubic phase, δ-Sb_2Te_3, with space group $Im\bar{3}m$ is observed where Sb and Te randomly occupy the same lattice site. Very recently, pressure-induced superconductivity has been observed in all phases above 4 GPa [73]. The microscopic lattice dynamics of α-, β- and γ-Sb_2Te_3 have been investigated thoroughly by nuclear inelastic scattering and inelastic neutron scattering [74] and Raman spectroscopy [72, 75]. The lattice dynamics of δ-Sb_2Te_3 is not accessible via Raman scattering due to the lack of Raman active modes in this phase caused by the mass disorder.
Here we report on the lattice dynamics of δ-$Sb_2\,{}^{125}Te_3$ at high pressure investigated by ^{121}Sb and ^{125}Te nuclear inelastic scattering which gives access to the element specific density of phonon states. The pressure dependences of several thermodynamical parameters are investigated. To our knowledge this is the first demonstration of pressure dependent ^{121}Sb and ^{125}Te nuclear inelastic scattering.

4.2 Experimental setup

The experiment was performed at the nuclear resonance beamline ID18 at the European Synchrotron Radiation Facility (ESRF). The storage ring was operated in the 16 bunch filling mode with an average beam current of 75 mA. The incident radiation of 35.49 keV for the ^{125}Te and of 37.13 keV for the ^{121}Sb nuclear resonances was monochromatized in two steps by a high-heat-load monochromator with Si (111) reflections followed by a high resolution sapphire backscattering monochromator [55] with a glancing angle of 89.93 ° in horizontal direction in order to separate the

direct and backscattered beam as required by the focussing optics and sample environment. Due to the relatively large horizontal beam divergence the resulting energy resolution was 1.7(1) meV and 3.3(2) meV for Te and Sb, respectively. The energy of the backscattered beam is tuned by adjusting the temperature of the sapphire crystal with mK precision. The beam after passing the backscattering monochromator was focused to a spot size of $24(2) \times 23(2)\,\mu\text{m}^2$ at the sample position using Kirkpatrick-Baez x-ray mirrors [76]. A panoramic diamond anvil cell of the Paderborn type, with large openings in the equatorial plane, was used [77]. The sample was loaded into a Be gasket with a $\sim 50\,\mu$m hole together with small ruby chips. The Be gasket ensures a minimal absorption of the nuclear fluorescence mostly consisting of $K_{\alpha,\beta}$ radiation. KCl was used as the pressure transmitting medium. The pressure was determined by using the ruby luminescence method and from the KCl lattice constant obtained from x-ray diffraction [78].

The radiation scattered from the sample coherently in forward direction was detected by a 16-element array of Si avalanche photodiodes (APD) [79]. The incoherently and isotropically scattered radiation originating from phonon-assisted nuclear resonant absorption was detected by two pairs of APDs perpendicular to the backscattered beam at a distance of less than 1 cm from the sample. The APDs have a time resolution of 0.5 ns and allow discrimination in time of the prompt electronic and delayed nuclear resonant scattering and fluorescence. The energy dependent and time integrated signal in forward direction gives the instrumental function of the monochromator while the incoherently scattered signal gives the absorption spectrum. The total acquisition time per spectrum was about 7 h.

X-ray diffraction was measured at the ESRF diffraction beamline ID09A using a wavelength of 0.414314 Å and the same panoramic diamond anvil cell and loading, without decompression, as for the nuclear inelastic scattering measurements in order to ensure comparability. The axial opening angle of this panoramic diamond anvil cell does not allow one to record the full diffraction pattern with the beam passing through the diamonds along the principal axis of the cell as is done for nuclear inelastic scattering. For that reason the beam was aligned perpendicular to the principal axis passing first through the Be gasket from the side and then through the sample yielding additional contributions from the Be gasket in the diffraction pattern. The FIT2D software was used to integrate the two dimensional diffraction patterns yielding 2Θ versus intensity plots [80, 81]. The DATLAB software [82] was used to extract the Bragg peak positions and the CHEKCELL software [83] to index the Bragg peaks and refine the lattice constants.

4.3 Experimental Method

Nuclear inelastic scattering of synchrotron radiation is based on the application of the Mössbauer effect and gives access to the element specific and momentum integrated density of phonon states of Mössbauer isotopes [23–25]. The technique will be only briefly discussed here and details can be found in [26]. The phonon absorption spectrum measured relative to the energy of the Mössbauer transition consists of an elastic scattering part, *i.e.* 0-phonon processes, and an inelastic scattering part, *i.e.* n-phonon processes. In order to correct for the elastic scattering contributions the instrumental function which is measured simultaneously is normalized to and subtracted from the raw absorption spectrum. A Fourier-Log decomposition is applied to expand the inelastic absorption spectrum in terms of one- and multi-phonon processes [27]. From the one-phonon

spectrum the density of phonon states is obtained. The consistency of this procedure is verified using Lipkin's sum rules which relate the raw absorption spectrum to the extracted density of phonon states [28, 29]. The DOS code is used to obtain the density of phonon states [84].

4.4 Sample preparation

$Sb_2\,^{125}Te_3$, 95 % ^{125}Te enriched, was synthesized from inductively melting a stoichiometric mixture of Sb and Te. The sample was polycrystalline and phase purity was confirmed by powder x-ray diffraction. The sample used for this study is from the same batch as the one used in [74].

4.5 Results and discussion

4.5.1 X-ray diffraction

The x-ray diffraction pattern of $Sb_2\,^{125}Te_3$ inside the diamond anvil cell was measured at 77(3) GPa. In order to exclude the contributions from the Be gasket several measurements at different positions next to the sample volume were performed. The obtained x-ray diffraction patterns of the $Sb_2\,^{125}Te_3$ and KCl inside the Be gasket and of the Be gasket itself are shown in Figure 4.1. The Debye-Scherrer rings of the Be gasket are split due to its relative large size and thus different focal planes. The measured Bragg peak positions of KCl and $Sb_2\,^{125}Te_3$ are listed in Table 4.1. The KCl Bragg

2Θ(°)			
(hkl)	δ-$Sb_2\,^{125}Te_3$	(hkl)	B2 KCl
011	10.2846(6)	011	11.15(1)
200	14.5696(3)	200	15.90(2)
022	20.57(2)	112	19.40(1)
013	23.05(2)	202	23.353(6)
222	25.39(2)	312	29.87(2)
033	31.189(7)		
323	34.59(2)		
134	37.771(7)		

Table 4.1: Extracted 2Θ Bragg peak positions of $Sb_2\,^{125}Te_3$ and KCl at 77(3) GPa. A wavelength of 0.414384 Å was used.

peaks can be clearly assigned to the B2 phase of KCl with the space group *Pm3m* and the lattice constant $a = 3.009(7)$ Å [78]. The pressure is determined using the Rydberg-Vinet equation of

state for B2 KCl,

$$P(V,T) = 3K_0\eta^{-2/3}(1-\eta^{1/3}) \cdot \exp\left[\frac{3}{2}(K_0^{'}-1)(1-\eta^{1/3})\right] + \overline{\alpha K_T}(T-300) \tag{4.5.1}$$

where $\eta = V/V_0$, $V_0 = 54.5\,\text{Å}^3$, $K_0 = 17.2\,\text{GPa}$, $K_0^{'} = 5.89$ and $\overline{\alpha K_T} = 2.24 \times 10^{-3}\,\text{GPa/K}$ [78]. We obtain a pressure of 77(3) GPa in agreement with the value obtained from the ruby luminescence method.

Three high pressure phases of Sb_2Te_3 have been observed up to 53 GPa [70, 71]. At $\sim$ 30 GPa Sb_2Te_3 transforms into a disordered body centred cubic phase with the space group $Im\bar{3}m$ where Sb and Te both randomly occupy the same lattice site. The measured Bragg peak positions of $Sb_2{}^{125}Te_3$ at 77(3) GPa can be clearly indexed to the cubic space group $Im\bar{3}m$ with the lattice constant $a = 3.268(4)$ Å and the normalized volume per Sb_2Te_3 formula unit $V/V_0 = 0.639(2)$ in agreement with the equation of state of δ-Sb_2Te_3 [70], see Figure 4.2. No secondary phase is observed, thus confirming the phase purity of the sample. The polycrystallinity of the sample is verified by the two-dimensional diffraction pattern revealing complete Debye-Scherrer rings. From the lattice constant and the number of formula units per unit cell, $n = 0.4$ [70], we calculate the density to be $\rho = 11.92(4)\,\text{g/cm}^3$.

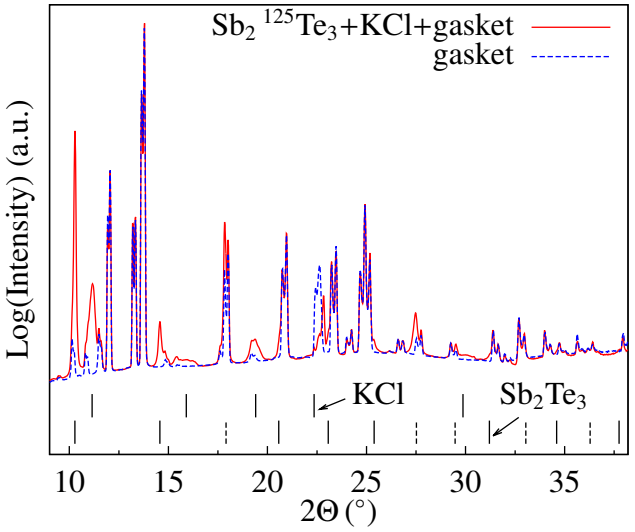

Figure 4.1: X-ray diffraction patterns of $Sb_2{}^{125}Te_3$ and KCl inside the Be gasket (solid line) and of the Be gasket itself (dashed line) obtained with a wavelength of 0.414384 Å at a pressure of 77(3) GPa. The extracted Sb_2Te_3 and KCl Bragg peak positions are marked by tics. δ-Sb_2Te_3 Bragg peaks hidden by the Be gasket contribution are marked by dashed tics. No secondary phase of Sb_2Te_3 is observed.

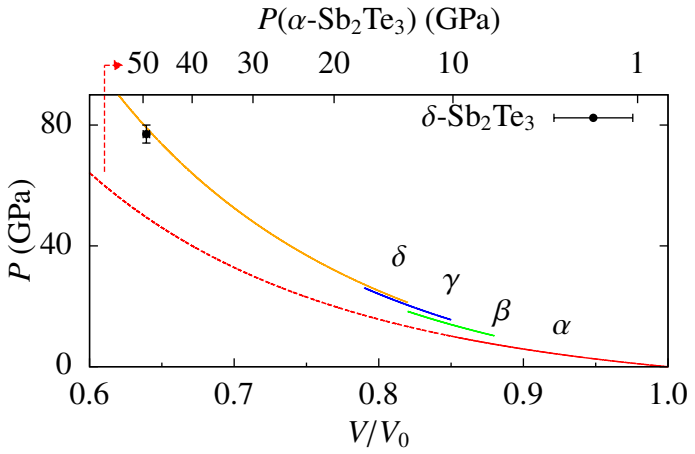

Figure 4.2: Equations of state of α-(red), β-(green), γ-(blue) and δ-(orange) Sb_2Te_3 adapted from [70], lines, and our measurement, point. Upper x-axis: equivalent pressure corresponding to the equation of state of α-Sb_2Te_3.

4.5.2 Nuclear inelastic scattering

The room temperature absorption spectra of ^{121}Sb and ^{125}Te in $Sb_2\,^{125}Te_3$ at 15(1) GPa and 77(3) GPa together with the instrumental functions are shown in Figure 4.3.

At 15(1) GPa only the absorption spectrum of ^{125}Te was measured and as the Lamb-Mössbauer factor of the sample was too small the instrumental function was obtained using a ^{125}Te sample at ambient pressure. The absorption spectrum reveals a broad distribution without recognizable phonon modes indicating strong multi-phonon contributions. This, in turn, hints at a very small Lamb-Mössbauer factor, f_{LM}, as the relative contribution of a n-phonon process to the absorption spectrum is given by $(-\ln f_{\mathrm{LM}})^n/n!$. From the inelastic absorption spectrum an upper bound of the Lamb-Mössbauer factor can be estimated according to

$$f_{\mathrm{LM}} = 1 - \int_{-\infty}^{\infty} W(E)dE, \tag{4.5.2}$$

where $W(E)$ is the normalized absorption spectrum corrected for the contribution of elastic scattering [26]. We obtain for the upper bound $f_{\mathrm{LM}} = 0.03(2)$. The decomposition of the inelastic absorption spectrum into a single-phonon and multi-phonon terms with such a low Lamb-Mössbauer factor is ambiguous [85] and the extraction of the density of phonon states was consequently not possible.

In the absorption spectra measured at 77(3) GPa we can clearly identify single-phonon modes, *e.g.* around 11 meV and 20 meV, and its decomposition into terms of single- and multi-phonon processes is possible. The extracted element specific densities of phonon states, $g(E)$, of ^{125}Te and ^{121}Sb and the full density of states of δ-Sb_2Te_3 are shown in Figure 4.4. In the low-energy, acoustic, part both densities of states are very similar and reveal two features at around 11 meV and 20 meV as already observed in the absorption spectra. In the high-energy, optical, part of the density of states we observe one phonon mode around 32 meV for Te and two modes around 26 meV and 36 meV for Sb. The density of states of α-Sb_2Te_3 obtained at ambient pressure and

20 K [74] is shown in Figure 4.4 on a different energy scale in order to compare it to the δ-phase at high pressure.

Typically, the shape of the density of phonon states remains similar under pressure, in a quasi-harmonic approximation, for the same crystallographic phase of materials [86] and only the cutoff energy increases with decreasing volume. However, only hardening of the density of phonon states is insufficient to describe the transformation between the α- and δ-phases of Sb_2Te_3. The strong optical phonon mode at 13 meV in the α-phase attributed to the vibrations of Te atoms along the c-direction [75] is absent in δ-Sb_2Te_3 which is expected for the phase transition from a layered rhombohedral to a cubic structure. δ-Sb_2Te_3 strongly resembles an amorphous material with respect to its mass disorder. The ^{125}Te and ^{121}Sb element specific and the total densities of states of amorphous $GeSb_2Te_4$ at ambient pressure and 25 K [12] which can be considered as a pseudo-binary compound of GeTe and Sb_2Te_3 are shown in Figure 4.4. The total densities of states of the δ-phase and amorphous $GeSb_2Te_4$ are very similar neglecting the different energy scales related to the different mass densities. Both show a broad peak in the acoustic part, a significant contribution close to the cutoff energy and a clear gap in between where the strong Te peak is observed in α-Sb_2Te_3. These similarities can be correlated to the bonding mechanism. In α-Sb_2Te_3 and crystalline $GeSb_2Te_4$ resonance bonding is prevalent [10, 87] whereas amorphous $GeSb_2Te_4$ is covalently bonded [10, 12]. This suggests that the bonding is predominantly covalent also in δ-Sb_2Te_3.

Thermodynamical parameters

From the density of phonon states a series of thermoydynamical parameters can be obtained [26]. We determined the Lamb-Mössbauer factor in δ-Sb_2Te_3 to be $f_{\mathrm{LM}} = 0.22(3)$ for both, ^{125}Te and ^{121}Sb, according to [88],

$$f_{\mathrm{LM}} = \exp\left(-E_R \int_0^\infty \frac{g(E)}{E} \frac{1+e^{-\beta E}}{1-e^{-\beta E}} dE\right), \tag{4.5.3}$$

where E_R is the recoil energy and $\beta = 1/(k_B T)$. The Lamb-Mössbauer factor is related to the incoherent atomic mean square displacement parameter by $\langle x^2 \rangle = -\ln(f_{\mathrm{LM}})/k_\gamma^2$ with the wave number, k_γ, of the nuclear transition. For ^{125}Te and ^{121}Sb we obtain $\langle x^2 \rangle = 4.7(4) \cdot 10^{-3}$ Å^2 and $\langle x^2 \rangle = 4.3(4) \cdot 10^{-3}$ Å^2, respectively. The Debye temperature, Θ_{D}, is calculated according to

$$\Theta_{\mathrm{D}}^2 = 3\left[k_B^2 \int_0^\infty g(E)/E^2 dE\right]^{-1}. \tag{4.5.4}$$

We obtain $\Theta_{\mathrm{D}} = 278(10)$ K and $\Theta_{\mathrm{D}} = 296(10)$ K for Te and Sb, respectively. The mean force constant, F, in the harmonic approximation is calculated to be $F = 214(30)$ N/m and

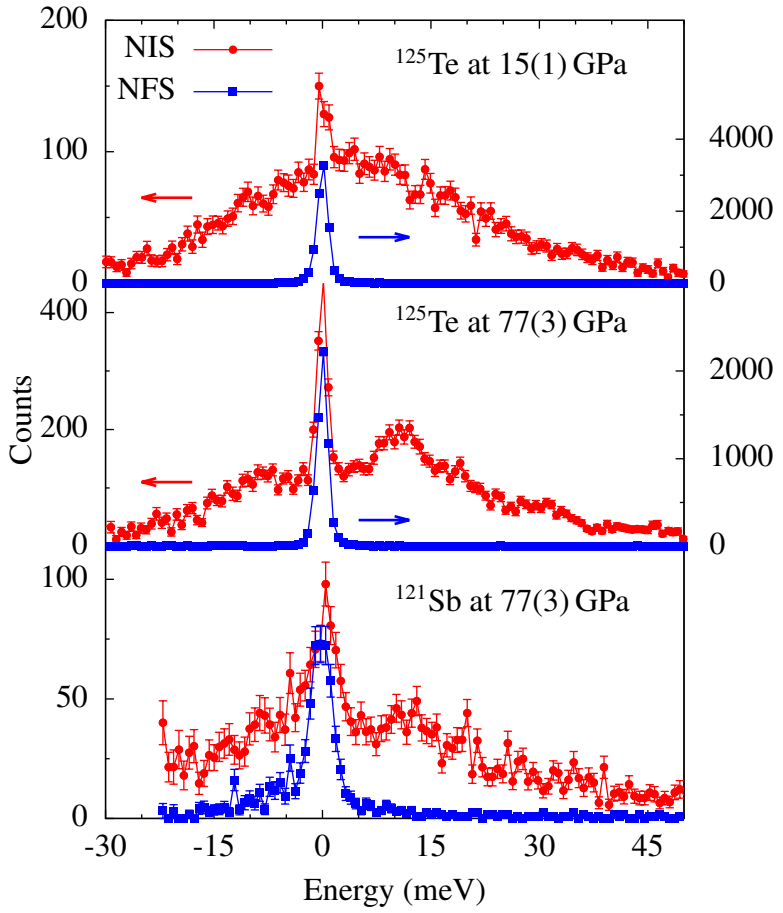

Figure 4.3: Nuclear inelastic absorption spectra (NIS) and instrumental functions (NFS) of ^{125}Te, measured at 15(1) and 77(3) GPa, and of ^{121}Sb, measured at 77(3) GPa, in $Sb_2\,^{125}Te_3$. Lines are guides to the eye.

$F = 275(30)$ N/m for Te and Sb, respectively, according to

$$F = M \int_0^\infty g(E)E^2 dE/\hbar^2, \tag{4.5.5}$$

with the mass, M, of the resonant nucleus. In the Debye approximation, the mean speed of sound is calculated from

$$v_s = \left(\frac{1}{2\pi^2\rho\hbar^3\alpha_\mathrm{D}}\right)^{1/3}, \tag{4.5.6}$$

with the Debye level per unit mass

$$\alpha_\mathrm{D} = \lim_{E\to 0}\frac{g(E)}{ME^2} \tag{4.5.7}$$

and the density ρ. The Debye level is obtained from the mass specific reduced density of states shown in Figure 4.4. The mean speed of sound, v_s, that corresponds to the long wavelength limit,

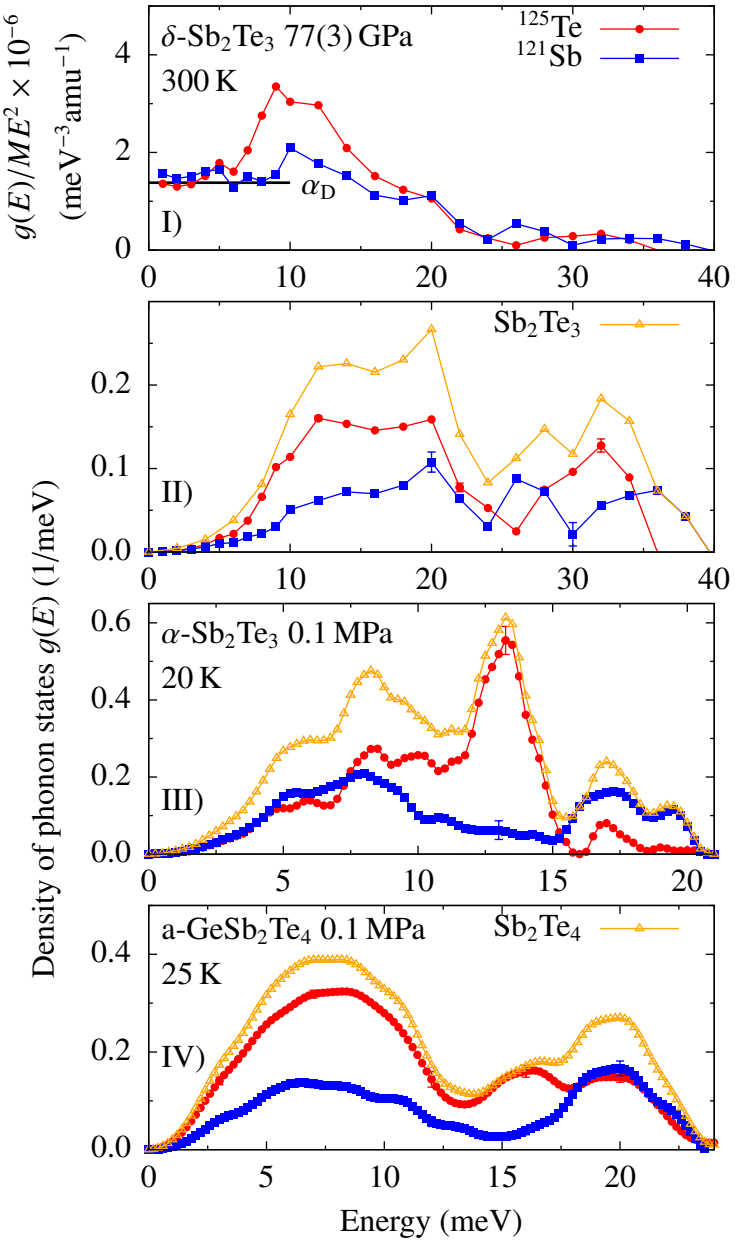

Figure 4.4: I): Mass specific reduced density of phonon states, $g(E)/ME^2$, of Te and Sb in Sb_2 $^{125}Te_3$ at 77(3) GPa. II-IV): Element specific and total densities of phonon states, $g(E)$, of Te and Sb in Sb_2 $^{125}Te_3$ at 77(3) GPa and 300 K and at ambient pressure and 20 K, adapted from [74], and in amorphous $GeSb_2Te_4$, adapted from [12], at ambient pressure and 25 K. The densities of states are normalized to the respective number of atoms per formula unit. For each material a different energy scale was used in order to match typical features. Lines are guides to the eye.

should not depend on the specific element. The mean Debye level per unit mass is determined to be $\alpha_D = 1.4(1) \cdot 10^{-6}\,\mathrm{meV^{-3}amu^{-1}}$ resulting in $v_s = 2.61(6)\,\mathrm{km/s}$. All extracted parameters are given in Table 4.2 together with the values for the ambient pressure phase [74].

	^{125}Te			^{121}Sb	
Pressure (GPa)	Ambient [74]	15(1)	77(3)	Ambient [74]	77(3)
f_{LM}	0.0089	0.03(2)	0.22(3)	0.0006	0.22(3)
$\langle x^2 \rangle$ (10^{-3}Å^2)	14.6	11(2)	4.7(4)	20.9	4.3(4)
F (N/m)	61(2)	-	214(30)	67(2)[a]	275(30)
Θ_{D} (K)	157(5)	-	278(10)	135(5)	296(10)
α_{D} (10^{-6}/meV^3/amu)	10.8(2)	-	1.4(1)[b]	-	1.4(1)[b]
v_s (km/s)	1.61(2)[a]	-	2.61(6)[b]	-	2.61(6)[b]
V per Sb_2Te_3 (Å^3)	159.9[c]	-	87.3(3)	159.9[c]	87.3(3)

Table 4.2: Lamb-Mössbauer factors, f_{LM}, atomic mean square displacement parameters, $\langle x^2 \rangle$, mean force constants, F, Debye temperatures, Θ_{D}, mean Debye level per unit mass, α_{D}, mean speed of sound, v_s, and volume per Sb_2Te_3 formula unit, V, at 15(1) GPa, 77(3) GPa and ambient pressure (adapted from [74]). [a] The value in [74] was wrongly calculated and is corrected here. [b] The mean Debye level and mean speed of sound are obtained from the Te and Sb densities of phonon states together. [c] Taken from [89].

The pressure dependence of the lattice dynamics yields mode specific Grüneisen parameters, γ_i. In general, such calculations are not correct taking the phase transition from α- to δ-Sb_2Te_3 into account. However, based on the similarity in shape of the ^{121}Sb density of phonon states at low and high pressure we assume that the Grüneisen parameter would be correct at least for this element. In order to generalize the calculations and apply them also to the ^{125}Te density of phonon states we use several moments of the density of phonon states which reproduce characteristic Debye cutoff energies and Grüneisen parameters for the low (acoustic) and high (optical) energy phonon modes, respectively. The mode specific Grüneisen parameter is defined as

$$\gamma_i \equiv -\frac{\partial \ln E_i}{\partial \ln V}, \tag{4.5.8}$$

where E_i is the energy of a phonon mode i and V is the volume per atom. In the simplest model, we assume the Grüneisen parameter of all phonon modes to be equal, $\gamma_i = \gamma$. Integration of Eq. (4.5.8) with the boundary conditions that at ambient pressure the energy of a phonon mode is E_0 and the volume per atom is V_0 yields for the phonon energy at pressure P

$$E(V) = E_0 \left(\frac{V_0}{V(P)} \right)^{\gamma} = E_0 \cdot a(V), \tag{4.5.9}$$

with $a(V) = \left(\frac{V_0}{V(P)}\right)^{\gamma}$. From Eq. (4.5.9) we can see that the energy of a phonon mode, E_0, is just scaled. The density of phonon states, $g'(E, V)$, at pressure P is then related to that at ambient pressure, $g(E, V_0)$, by

$$g'(E, V) = \frac{g(E/a(V), V_0)}{a(V)}. \tag{4.5.10}$$

The Debye cutoff energy of n-th order is defined as [90–92]

$$E_{(n)} = \left(\frac{n+3}{3} \langle E^n \rangle \right)^{1/n}, \tag{4.5.11}$$

where $\langle E^n \rangle$ is the n-th moment of the density of phonon states

$$\langle E^n \rangle = \int_0^\infty g(E) E^n dE \quad \text{with } n \neq 0, n > -3. \tag{4.5.12}$$

$E_{(0)}$ is defined as

$$E_{(0)} = \exp\left(1/3 + \int_0^\infty g(E) \ln(E) dE \right). \tag{4.5.13}$$

$E_{(-3)}$ is obtained according to

$$E_{(-3)} = \left(\frac{1}{3} \lim_{E \to 0} \frac{g(E)}{E^2} \right)^{-1/3}. \tag{4.5.14}$$

In general, $E_{(n)}$ is the characteristic Debye cutoff energy of a Debye-like density of phonon states yielding the same n-th moment as the real density of phonon states [92]. For specific values of n these Debye energies give the equivalent Debye characteristic energies obtained by different experimental methods [92]: $E_{(-3)}$ and $E_{(2)}$ are the equivalent Debye energies obtained from the temperature dependence of the heat capacity in the low and high temperature limits, respectively. Comparing Eqs. (4.5.6) and (4.5.14) indicates that $E_{(-3)}$ is also related to the speed of sound. $E_{(-1)}$ and $E_{(-2)}$ are the equivalent Debye energies obtained from the temperature dependence of the atomic displacement parameter in the low and high temperature limits, respectively. Combining Eqs. (4.5.10) and (4.5.11-4.5.14) we obtain the characteristic Grüneisen parameter of n-th moment, $\gamma_{(n)}$, [92]

$$\ln \frac{E_{(n)}(V)}{E_{(n)}(V_0)} = -\gamma_{(n)} \ln \frac{V}{V_0}. \tag{4.5.15}$$

These characteristic Grüneisen parameters $\gamma_{(n)}$ are related to the macroscopic Grüneisen parameter, γ_G, defined as $\gamma_G \equiv -\alpha_V/(K_T c_V)$ with the volume expansion coefficient, α_V, the isothermal compressibility, K_T, and the specific heat at constant volume, c_V. Especially, $\gamma_{(0)}$ and $\gamma_{(-3)}$ are the high and low temperature limits of γ_G [92]. The Grüneisen parameters calculated using the data in Table 4.2 and Eq. (4.5.15) are presented in Table 4.3 together with the macroscopically determined Grüneisen parameter, γ_G, taken from Ref. [74]. $E_{(-3)}$ of Sb in α-Sb_2Te_3 cannot be determined from the data in [74]. For Sb we observe a clear decrease of the Grüneisen parameter with increasing order, n, corresponding to a stronger weight on the high energy phonon modes. Thus, the high energy phonon modes are less affected by pressure in agreement with Raman spectroscopy results [72, 75]. This verifies our assumption above that the calculation of the Grüneisen parameter for Sb is valid despite the phase transition from α- to δ-Sb_2Te_3. On the other hand, due to this assumption we obtain slightly underestimated Grüneisen parameters compared to the macroscopically deter-

	Te	Sb
$\gamma_{(-3)}$	1.16(8)	-[a]
$\gamma_{(-2)}$	0.96(8)	1.32(8)
$\gamma_{(-1)}$	0.92(8)	1.29(8)
$\gamma_{(0)}$	0.95(8)	1.26(7)
$\gamma_{(1)}$	1.00(7)	1.21(7)
$\gamma_{(2)}$	1.04(7)	1.16(7)
γ_G	1.7(1)	

Table 4.3: Characteristic Grüneisen parameters, $\gamma_{(n)}$, of n-th order obtained from equation (4.5.15) and the data in Table 4.2 and the macroscopically determined Grüneisen parameter, γ_G, taken from [74]. [a] $E_{(-3)}$ of Sb in α-Sb_2Te_3 could not be determined.

mined Grüneisen parameter, γ_G. For Te we observe only a marginal increase, within errorbars, of the Grüneisen parameter with increasing order n, except for $n = -3$, and overall smaller values than for Sb. Compared to the macroscopically determined Grüneisen parameter our values are much smaller. This is related to the influence of the phase transition on the Te vibrations and shows that neglecting the phase transitions undermines our capacity to reliably determine the Grüneisen parameter for Te.

In the Debye approximation, the Lamb-Mössbauer factor is a function of the Debye temperature and the temperature [14]. Combining Eqs. (4.5.4) and (4.5.10) we obtain for the Lamb-Mösbauer factor

$$f_{\mathrm{LM}}(V, T, \Theta_{\mathrm{D}}) = f_{\mathrm{LM}}(V_0, T, a(V)\Theta_{\mathrm{D}}). \tag{4.5.16}$$

Thus, increasing pressure is similar to increasing the Debye temperature of the material. In Figure 4.5, the Lamb-Mössbauer factors of ^{125}Te and ^{121}Sb in α- and δ-Sb_2Te_3 are depicted as a function of temperature at 8 GPa and 77(3) GPa, respectively, where $a(V)$ was calculated from the equation of state [70] and with the macroscopically determined Grüneisen parameter, $\gamma_G = 1.7(1)$, assumed here to be temperature-independent. Taking a Lamb-Mössbauer factor of $f_{\mathrm{LM}} = 0.2$ as a threshold for the feasibility of nuclear inelastic scattering and the extraction of the density of phonon states we can conclude that in order to reliably determine $g(E)$ near the α-β phase transition at $\sim$ 8 GPa temperatures below 145 K and 103 K are necessary for Te and Sb, respectively. At room temperature, nuclear inelastic scattering by ^{125}Te and ^{121}Sb is feasible above 27 GPa and 49 GPa, respectively.

4.6 Conclusion

We measured ^{121}Sb and ^{125}Te nuclear inelastic scattering in $Sb_2{}^{125}Te_3$ at 15(1) GPa and 77(3) GPa. We extracted the element specific density of phonon states of δ-$Sb_2{}^{125}Te_3$ at 77(3) GPa. The to-

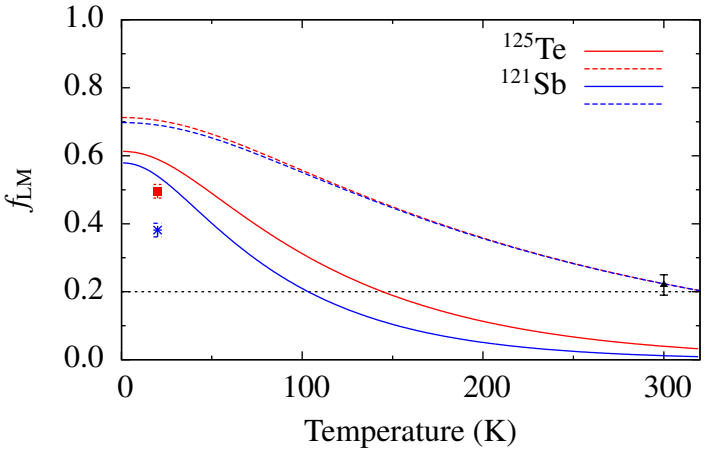

Figure 4.5: ^{125}Te (red) and ^{121}Sb (blue) Lamb-Mössbauer factors, f_{LM}, of α-Sb_2Te_3 (solid line) at 8 GPa and of δ-Sb_2Te_3 (dashed line) at 77(3) GPa as a function of temperature. The red and blue data points indicate the conditions at which the densities of states of α-Sb_2Te_3 at ambient pressure were measured (see Figure (4.4.III) and Ref. [74]).

tal density of phonon states of the δ-phase strongly resembles the one of amorphous $GeSb_2Te_4$ suggesting a covalent bonding mechanism in contrast to the resonance bonding in α-Sb_2Te_3. Using a simple model with a mode-independent Grüneisen parameter we calculated characteristic Grüneisen parameters from several moments of the density of phonon states. The Sb high energy phonon modes are less effected by pressure. On average we obtain Grüneisen parameters of $\overline{\gamma} = 1.25(3)$ and $\overline{\gamma} = 1.01(3)$ for Sb and Te, respectively. Pressure dependent ^{121}Sb and ^{125}Te nuclear inelastic scattering at room temperature and the extraction of the density phonon states in Sb_2Te_3 are feasible above 49 GPa and 27 GPa, respectively. The pressure dependence of the lattice dynamics of technologically more relevant α-Sb_2Te_3 might shed light on mechanisms for thermal transport in this phase. In order to study α-Sb_2Te_3 around 8 GPa using nuclear inelastic scattering temperatures below 145 K and 103 K will be necessary for Te and Sb, respectively.

4.7 Acknowledgements

The authors acknowledge the European Synchrotron Radiation Facility for the provision of beam time at ID18 and ID09, R. Rüffer and M. Herlitschke for their support during the experiment, the financial support by the Deutsche Forschungsgemeinschaft within the SFB917 "Nanoswitches" and by the Helmholtz-Gemeinschaft deutscher Forschungszentren within VH-NG-407.

Chapter 5

5

Element resolved lattice dynamics in the $SnSb_2Te_4$ phase change material

Abstract

The element specific densities of phonon states in the phase change material $SnSb_2Te_4$ in the amorphous, cubic and hexagonal phases were determined using nuclear inelastic scattering by the ^{119}Sn, ^{121}Sb and ^{125}Te Mössbauer isotopes. For all three elements the densities of phonon states reveal a hardening upon crystallization in the acoustic range corresponding to an increase in speed of sound and Debye temperatures and a decrease in atomic mean square displacement parameters. In contrast, with the onset of resonance bonding upon crystallization, a softening of the high energy optical phonon modes is observed for Sb and Te but not for Sn suggesting that there might be no change in bonding mechanism for Sn. Strong similarities between the Sb and Te densities of phonon states of amorphous $SnSb_2Te_4$ and $GeSb_2Te_4$ suggest the same structural environment in both compounds. Several vibrational and thermodynamical parameters are derived from the densities of phonon states. The change in the vibrational entropy upon crystallization is interpreted within the picture of resonance bonding. Investigation of the element specific vibrational entropy at room temperature suggests that the amorphous to cubic phase transition is driven by Sb and Te but hampered by Sn.

R. E. Simon[1,2], J. Gallus[1], I. Sergueev[3], G. Bruns[4,5], M. Wuttig[4,5] and R. P. Hermann[1,2]

[1] *Jülich Centre for Neutron Science JCNS and Peter Grünberg Institut PGI, JARA-FIT, Forschungszentrum Jülich GmbH, D-52425 Jülich, Germany*

[2] *Faculté des Sciences, Université de Liège - B-4000 Liège, Belgium*

[3] *Deutsches Elektronen-Synchrotron - D-22607 Hamburg, Germany*

[4] *I. Physikalisches Institut (IA), RWTH Aachen University, D-52056, Aachen, Germany*

[5] *JARA - Fundamentals of Information Technology, RWTH Aachen University, D-52056 Aachen, Germany*

Chapter 6

6

Inelastic X-ray scattering by the phase change materials $GeSb_2Te_4$ and $Ge_2Sb_2Te_5$

Abstract

The generalized density of phonon states is determined from inelastic X-ray scattering by the phase change materials $GeSb_2Te_4$ and $Ge_2Sb_2Te_5$ in the as deposited amorphous and crystalline, rock-salt phases. A simultaneous hardening in the acoustic and softening in the optical phonon range is revealed upon crystallization, in line with previous nuclear inelastic and inelastic neutron scattering studies, and corresponds to the change in bonding mechanism from ordinary covalent to resonance bonding. By combining the X-ray generalized densities of phonon states with published neutron generalized and Sb and Te partial densities of phonon states access to the Ge specific lattice dynamics was enabled. The Ge partial densities of phonon states reveal the existence of high energy phonon modes in the as deposited phase, modes that are most probably related to tetrahedrally coordinated Ge atoms and that almost completely vanish upon crystallization. Upon structurally relaxing the as deposited samples by thermal annealing below the crystallization temperature no significant changes in the generalized densities of phonon states are observed, particularly concerning tetrahedrally coordinated Ge.

R. E. Simon[1,2], F. Lange[3,4], B. Wehinger[5], S. Jakobs[3,4], M. Wuttig[3,4] and R. P. Hermann[1,2]

[1] *Jülich Centre for Neutron Science JCNS and Peter Grünberg Institut PGI, JARA-FIT, Forschungszentrum Jülich GmbH, D-52425 Jülich, Germany*

[2] *Faculté des Sciences, Université de Liège - B-4000 Liège, Belgium*

[3] *I. Physikalisches Institut (IA), RWTH Aachen University, D-52056, Aachen, Germany*

[4] *JARA - Fundamentals of Information Technology, RWTH Aachen University, D-52056 Aachen, Germany*

[5] *European Synchrotron Radiation Facility, BP 220, F-38043 Grenoble, France*

Chapter 7

7

Microscopic fingerprinting of resonance bonding in phase change materials by ^{121}Sb Mössbauer spectroscopy

Abstract

We performed ^{121}Sb Mössbauer spectral measurements on a variety of Sb-based phase change materials, namely Ge-Sb-Te, Sn-Sb-Te and (Ag-In)-Sb-Te in order to investigate differences in the microscopic bonding properties between the amorphous and crystalline phase. The Sb valence electron configuration is determined from the isomer shift using tight binding calculations. A common feature observed upon crystallization is a significant change in the number of Sb 5p electrons which relates to the onset of resonance bonding and the corresponding pronounced delocalization of electrons that is characteristic for this bonding mechanism. Our results provide strong microscopic evidence for resonance bonding in crystalline phase change materials and establish ^{121}Sb Mössbauer spectroscopy as a fingerprinting technique for resonance bonding.

R. E. Simon[1,2], A. Mahmoud[1], F. Lange[3,4], M. Wuttig[3,4], D. E. Brown[5], E. E. Alp[6] and R. P. Hermann[1,2]

[1] *Jülich Centre for Neutron Science JCNS and Peter Grünberg Institut PGI, JARA-FIT, Forschungszentrum Jülich GmbH, D-52425 Jülich, Germany*

[2] *Faculté des Sciences, Université de Liège - B-4000 Liège, Belgium*

[3] *I. Physikalisches Institut (IA), RWTH Aachen University, D-52056, Aachen, Germany*

[4] *JARA - Fundamentals of Information Technology, RWTH Aachen University, D-52056 Aachen, Germany*

[5] *Physics Department, Northern Illinois University, DeKalb, Illinois 60115, USA*

[6] *Advanced Photon Source, Argonne National Laboratory, Argonne, Illinois 60439, USA*

Chapter 8

8 Summary and outlook

In thesis, the lattice dynamics of phase change materials have been studied using several different approaches. Phonon spectroscopy methods were applied in order to determine the density of phonon states and Mössbauer spectroscopy was used in order to investigate the bonding properties of phase change materials.

Within the scope of this thesis the technique of nuclear resonance scattering was further developed in two ways. First, the experimental capabilities of nuclear forward scattering have been extended to the Mössbauer isotope ^{73}Ge. The influence of chemical bonding on the isomer shift has been investigated on ideal model systems, namely the tetravalent Ge compounds $CaGeO_3$ and in GeO_2 in various crystalline phases characterized by four-, mixed four/six- and six-fold Ge coordination, the divalent Ge compounds GeS and GeSe and pure Ge. The measurements of the isomer shift revealed a clear dependence on the Ge valence state but no direct dependence of the isomer shift on the Ge coordination geometry. The Ge specific lattice dynamics of these compounds were investigated by determining Lamb-Mössbauer factors and Debye temperatures. Quadrupole and magnetic hyperfine interactions, however, have proven elusive to this technique. A range for the so far unknown magnetic moment of the excited state of ^{73}Ge could be determined.
Though no phase change materials were investigated, in particular, these measurements must be considered as a prerequisite for any further Ge specific Mössbauer spectral studies on Ge bearing phase change materials. The importance of these measurements is underlined by the results that were obtained in this thesis by ^{121}Sb Mössbauer spectroscopy revealing a clear fingerprint for resonance bonding, namely the significant change in the Sb valence electron configuration, which makes the established relation between isomer shift and Ge valence state even more valuable for further studies.

Second, the feasibility of nuclear inelastic scattering by ^{121}Sb and ^{125}Te under high pressure has been demonstrated at room temperature on the prototypical phase change material Sb_2Te_3 up to 77 GPa. The full density of phonon states of the high pressure δ-phase of Sb_2Te_3 resembles that of amorphous $GeSb_2Te_4$ thus suggesting a covalent bonding mechanism in contrast to resonance bonding which is present in the ambient pressure α-phase of Sb_2Te_3. The determination of the Grüneisen parameter from various moments of the density of phonon states revealed that the Sb high energy phonon modes are less affected by pressure. On the basis of the Lamb-Mössbauer factor estimates of the minimal pressure necessary for ^{121}Sb and ^{125}Te nuclear inelastic scattering measurements at room temperature are given.
In order to further study phase change materials in the relevant pressure range of $1 - 20$ GPa where pressure-induced amorphization occurs, simultaneous cooling of the samples to approximately 100 K will be necessary. These measurements will provide not only insights into the microscopic

mechanisms leading to pressured-induced amorphization but also into the lattice anharmonicity of phase change materials. Determination of mode specific Grüneisen parameters characterizing the degree of anharmonicity is compelling as the low thermal conductivity of phase change materials, especially in the crystalline phase, is in part related to a strong lattice anharmonicity.

Two model systems of phase change materials, Sn-Sb-Te and Ge-Sb-Te, were studied with respect to their vibrational properties in terms of the density of phonon states using phonon spectroscopy methods.
The element resolved lattice dynamics of the $SnSb_2Te_4$ phase change material in the amorphous and two crystalline phases, cubic and hexagonal, have been determined using ^{119}Sn, ^{121}Sb and ^{125}Te nuclear inelastic scattering. The densities of phonon states of crystalline $SnSb_2Te_4$ resembles those of SnTe and Sb_2Te_3 which underlines the strong structural similarities between the compounds. Amorphous $SnSb_2Te_4$ and $GeSb_2Te_4$ reveal almost equal Sb and Te densities of phonon states thus suggesting the same structural environments in both phases. Upon crystallization the densities of phonon states of all three elements reveal a hardening in the acoustic phonon range quantified by larger Debye temperatures and smaller atomic displacement parameters. At the same time, the densities of phonon states of Sb and Te reveal a softening upon crystallization in the optical phonon range in accordance with the change from covalent to resonance bonding. In contrast, the Sn density of phonon states reveals hardly any softening suggesting the same bonding mechanism for Sn in the amorphous and crystalline phase. Differences in the vibrational entropy between the amorphous and crystalline phases are explained by the onset of resonance bonding. Further, the element specific vibrational entropies suggest that the transition from the amorphous to the cubic phase is driven by Sb and Te but hampered by Sn. The softening of the Sb but not the Sn densities of phonon states upon crystallization must be considered as contrasting with molecular dynamics simulations of Ge-Sb-Te which revealed the opposite effect.

The generalized densities of phonon states of $GeSb_2Te_4$ and $Ge_2Sb_2Te_5$ in the amorphous and cubic phases were determined using inelastic X-ray scattering and revealed a simultaneous hardening and softening in the acoustic and optical phonon range, respectively, upon crystallization. The results are in line with previous lattice dynamical studies. Access to the Ge specific lattice dynamics was enabled by combining the inelastic X-ray scattering with inelastic neutron and nuclear inelastic scattering data. A similar softening of the Ge phonons as for Sb and Te is observed. The existence of high energetic Ge phonon modes in the amorphous phase is revealed, modes that almost completely vanish upon crystallization and that are most probably related to tetrahedrally coordinated Ge. Structural relaxation of the as deposited amorphous samples by thermal annealing does not cause a reduction in spectral weight of these high energetic Ge phonon mode, however, further studies on differently relaxed samples are necessary to confirm this. The softening of the Ge density of phonon states must be contrasted with the results obtained for the isovalent phase change material $SnSb_2Te_4$ which revealed hardly any softening of the Sn density of phonon states.

The bonding properties of several phase change materials, namely Ge/Sn-Sb-Te, AIST and In_3SbTe_2, have been investigated using ^{121}Sb Mössbauer spectroscopy. From the measured isomer shift the Sb valence configuration was determined using tight binding calculations. The measurements reveal a significant change in isomer shift which is common for all compounds and clearly related to a change in the number of Sb 5p-electrons. The proposed change from ordinary covalent in the amorphous to resonance bonding in the crystalline phase with the concomitant electron delocalization gives a full explanation for the change in Sb electron configuration. Taking the

differences in electronegativity between the constituting elements into account the magnitude as well as the direction of the change in the number of Sb 5p-electrons can be explained. The results provide strong evidence for the change in bonding mechanism and establish ^{121}Sb Mössbauer spectroscopy as a fingerprinting technique for resonance bonding.
A systematic ^{119}Sn and ^{125}Te Mössbauer spectroscopy study should be carried out to further investigate the impact of the changes in the Sb valence electron configuration on the corresponding bonding partners. In addition, ^{73}Ge nuclear forward scattering can provide valuable information about the Ge valence state.

Bibliography

[1] S. Hudgens and B. Johnson, *MRS Bulletin*, 2004, **29**, 829–832.

[2] M. Wuttig and N. Yamada, *Nat Mater*, 2007, **6**, 824–832.

[3] D. Lencer, M. Salinga and M. Wuttig, *Adv. Mater.*, 2011, **23**, 2030–2058.

[4] M. Wuttig, *Phys. Status Solidi B*, 2012, **249**, 1843–1850.

[5] N. Yamada, *MRS Bulletin*, 1996, **21**, 48–50.

[6] T. Matsunaga, H. Morita, R. Kojima, N. Yamada, K. Kifune, Y. Kubota, Y. Tabata, J.-J. Kim, M. Kobata, E. Ikenaga and K. Kobayashi, *Journal of Applied Physics*, 2008, **103**, 093511.

[7] H. Iwasaki, M. Harigaya, O. Nonoyama, Y. Kageyama, M. Takahashi, K. Yamada, H. Deguchi and Y. Ide, *Japanese Journal of Applied Physics*, 1993, **32**, 5241–5247.

[8] Y. Maeda, H. Andoh, I. Ikuta and H. Minemura, *Journal of Applied Physics*, 1988, **64**, 1715–1719.

[9] M. Wuttig, D. Lusebrink, D. Wamwangi, W. Welnic, M. Gilleszen and R. Dronskowski, *Nat Mater*, 2007, **6**, 122–128.

[10] K. Shportko, S. Kremers, M. Woda, D. Lencer, J. Robertson and M. Wuttig, *Nat Mater*, 2008, **7**, 653–658.

[11] L. Pauling, *Nature Of the Chemical Bond*, Cornell. Univ. Press, 1939.

[12] T. Matsunaga *et al.*, *Adv. Funct. Mater.*, 2011, **21**, 2232–2239.

[13] S. Lee, K. Esfarjani, T. Luo, J. Zhou, Z. Tian and G. Chen, *Nat. Commun.*, 2014, **5**, 3525.

[14] P. Gütlich, E. Bill and A. X. Trautwein, *Mössbauer Spectroscopy and Transition Metal Chemistry*, Springer Berlin Heidelberg, 2011.

[15] R. L. Mössbauer, *Zeitschrift für Physik*, 1958, **151**, 124–143.

[16] R. L. Mössbauer, *Naturwissenschaften*, 1958, **45**, 538–539.

[17] R. L. Mössbauer, *Zeitschrift für Naturforschung Part A-Astrophysik Physik Und Physikalische Chemie*, 1959, **14**, 211–216.

[18] P. Jernberg, L. Häggström and T. Sundqvist, *Physica Scripta*, 1985, **31**, 215–216.

[19] S. S. Al-Dargazelli and M. M. Elias, *International Journal of Radiation Applications and Instrumentation. Part A. Applied Radiation and Isotopes*, 1989, **40**, 421–424.

[20] S. Ohya, *Nuclear Data Sheets*, 2010, **111**, 1619–1806.

[21] P. Lippens, *Solid State Communications*, 2000, **113**, 399–403.

[22] R. Röhlsberger, *Nuclear Condensed Matter Physics with Synchrotron Radiation - Basic Principles, Methodology and Applications*, Springer Berlin Heidelberg, 2005.

[23] M. Seto, Y. Yoda, S. Kikuta, X. W. Zhang and M. Ando, *Phys. Rev. Lett.*, 1995, **74**, 3828–3831.

[24] W. Sturhahn, T. S. Toellner, E. E. Alp, X. Zhang, M. Ando, Y. Yoda, S. Kikuta, M. Seto, C. W. Kimball and B. Dabrowski, *Phys. Rev. Lett.*, 1995, **74**, 3832–3835.

[25] A. I. Chumakov, R. Rüffer, H. Grünsteudel, H. F. Grünsteudel, G. Grübel, J. Metge, O. Leupold and H. A. Goodwin, *EPL (Europhysics Letters)*, 1995, **30**, 427–432.

[26] R. Rüffer and A. I. Chumakov, *Hyperfine Interactions*, 2000, **128**, 255–272.

[27] D. W. Johnson and J. C. H. Spence, *Journal of Physics D: Applied Physics*, 1974, **7**, 771–780.

[28] H. J. Lipkin, *Annals of Physics*, 1960, **9**, 332–339.

[29] H. J. Lipkin, *Phys. Rev. B*, 1995, **52**, 10073–10079.

[30] E. Burkel, *Reports on Progress in Physics*, 2000, **63**, 171–232.

[31] M. Krisch and F. Sette, *Topics in Applied Physics*, Springer Berlin Heidelberg, 2007, vol. 108, pp. 317–370.

[32] A. Bosak and M. Krisch, *Phys. Rev. B*, 2005, **72**, 224305.

[33] S. Balraj, *Nuclear Data Sheets*, 2004, **101**, 193–323.

[34] G. Czjzek *et al.*, *Physics Letters*, 1966, **19**, 673–675.

[35] G. Czjzek *et al.*, *Phys. Rev.*, 1968, **174**, 331–345.

[36] B. H. Zimmermann *et al.*, *physica status solidi (b)*, 1968, **27**, 639–651.

[37] R. S. Raghavan and L. Pfeiffer, *Phys. Rev. Lett.*, 1974, **32**, 512–514.

[38] A. Svane and E. Antoncik, *Hyperfine Interactions*, 1986, **30**, 145–152.

[39] A. V. Kolobov *et al.*, *Nat Mater*, 2004, **3**, 703–708.

[40] D. A. Baker *et al.*, *Phys. Rev. Lett.*, 2006, **96**, 255501.

[41] L. Pfeiffer and T. Kovacs, *Phys. Rev. B*, 1981, **23**, 5725–5728.

[42] M. Seto *et al.*, *Phys. Rev. Lett.*, 2009, **102**, 217602.

[43] J. B. Hastings, D. P. Siddons, U. van Bürck, R. Hollatz and U. Bergmann, *Phys. Rev. Lett.*, 1991, **66**, 770–773.

[44] I. Sergueev *et al.*, *Phys. Rev. Lett.*, 2007, **99**, 097601.

[45] I. Sergueev *et al.*, *Phys. Rev. Lett.*, 2013, **111**, 157601.

[46] Y. Shvyd'ko, *Hyperfine Interactions*, 2000, **125**, 173–188.

[47] V. K. Michaelis and S. Kroeker, *J. Phys. Chem. C*, 2010, **114**, 21736–21744.

[48] T. Whitfield *et al.*, *Journal of Solid State Chemistry*, 2003, **175**, 13 – 19.

[49] S. Sasaki, C. T. Prewitt and R. C. Liebermann, *American Mineralogist*, 1983, **68**, 1189–1198.

[50] A. Nakatsuka, H. Chaya and A. Yoshiasa, *American Mineralogist*, 2005, **90**, 755–757.

[51] J. Barbier and D. Lèvy, *Zeitschrift für Kristallographie*, 1997, **212**, 519–528.

[52] J. Haines, O. Cambon, E. Philippot, L. Chapon and S. Hull, *Journal of Solid State Chemistry*, 2002, **166**, 434–441.

[53] A. A. Bolzan *et al.*, *Acta Crystallographica Section B*, 1997, **53**, 373–380.

[54] C. Kittel, *Introduction to Solid State Physics*, Wiley, 2005.

[55] I. Sergueev, H.-C. Wille, R. P. Hermann, D. Bessas, Y. V. Shvyd'ko, M. Zajac and R. Rüffer, *Journal of Synchrotron Radiation*, 2011, **18**, 802–810.

[56] W. Makulski *et al.*, *J. Phys. Chem. A*, 2006, **110**, 11462–11466.

[57] H. Yamamoto, *Journal of the Physical Society of Japan*, 1965, **20**, 2166–2169.

[58] P. Schobinger-Papamantellos *et al.*, *Journal of Alloys and Compounds*, 1996, **232**, 165 – 168.

[59] Y.-L. Chen and D.-P. Yang, *Mössbauer Effect in Lattice Dynamics*, Wiley, 2007.

[60] M. Cordey-Hayes, *Journal of Inorganic and Nuclear Chemistry*, 1964, **26**, 915–923.

[61] R. Kurian and M. Filatov, *J. Chem. Phys.*, 2009, **130**, 124121.

[62] P. Lippens, J. Olivier-Fourcade and J. Jumas, *Hyperfine Interactions*, 2000, **126**, 137–141.

[63] D. Andrault *et al.*, *Physics and Chemistry of Minerals*, 1992, **18**, 506–513.

[64] A. Yoshiasa *et al.*, *Journal of Synchrotron Radiation*, 1999, **6**, 1051–1058.

[65] A. Yoshiasa *et al.*, *Journal of Synchrotron Radiation*, 2001, **8**, 940–942.

[66] R. J. Mehta, Y. Zhang, C. Karthik, B. Singh, R. W. Siegel, T. Borca-Tasciuc and G. Ramanath, *Nat Mater*, 2012, **11**, 233.

[67] H. Zhang, C. Liu, X. Qi, X. Dai, Z. Fang and S. Zhang, *Nature Physics*, 2009, **5**, 438.

[68] N. Ashcroft and N. Mermin, *Solid state physics*, Saunders College, 1976.

[69] M. K. Jacobsen, S. V. Sinogeikin, R. S. Kumar and A. L. Cornelius, *Journal of Physics and Chemistry of Solids*, 2012, **73**, 1154–1158.

[70] J. Zhao, H. Liu, L. Ehm, Z. Chen, S. Sinogeikin, Y. Zhao and G. Gu, *Inorg. Chem.*, 2011, **50**, 11291–11293.

[71] Y. Ma, G. Liu, P. Zhu, H. Wang, X. Wang, Q. Cui, J. Liu and Y. Ma, *Journal of Physics: Condensed Matter*, 2012, **24**, 475403.

[72] S. Souza, C. Poffo, D. Trichês, J. de Lima, T. Grandi, A. Polian and M. Gauthier, *Physica B: Condensed Matter*, 2012, **407**, 3781–3789.

[73] J. Zhu *et al.*, *Sci. Rep.*, 2013, **3**, 2016.

[74] D. Bessas, I. Sergueev, H.-C. Wille, J. Perßon, D. Ebling and R. P. Hermann, *Phys. Rev. B*, 2012, **86**, 224301.

[75] O. Gomis, R. Vilaplana, F. J. Manjón, P. Rodríguez-Hernández, E. Pédro M. Aguiarrez-González, A. Muñoz, V. Kucek and C. Drasar, *Phys. Rev. B*, 2011, **84**, 174305.

[76] P. Kirkpatrick and A. V. Baez, *J. Opt. Soc. Am.*, 1948, **38**, 766–773.

[77] R. Lübbers, H. F. Grünsteudel, A. I. Chumakov and G. Wortmann, *Science*, 2000, **287**, 1250–1253.

[78] A. Dewaele, A. B. Belonoshko, G. Garbarino, F. Occelli, P. Bouvier, M. Hanfland and M. Mezouar, *Phys. Rev. B*, 2012, **85**, 214105.

[79] A. Baron, *Hyperfine Interactions*, 2000, **125**, 29–42.

[80] A. P. Hammersley, *FIT2D: An Introduction and Overview"*, ESRF Internal Report, ESRF97HA02T, 1997.

[81] A. P. Hammersley, S. O. Svensson, M. Hanfland, A. N. Fitch and D. Hausermann, *High Pressure Research*, 1996, **14**, 235–248.

[82] K. Syassen, *Computer code DATLAB*, Max-Planck-Institute, Stuttgart, Germany, 2001.

[83] J. Laugier and B. Bochu, *Powder Indexing Helper Tool for Unit Cell and Spacegroup Assignment*, Laboratoire des Matériaux et du Génie Physique (LMPG), France, version 11.01.2004.

[84] V. G. Kohn and A. I. Chumakov, *Hyperfine Interactions*, 2000, **125**, 205–221.

[85] B. Klobes, A. Desmedt, I. Sergueev, K. Schmalzl and R. P. Hermann, *EPL (Europhysics Letters)*, 2013, **103**, 36001.

[86] C. A. Murphy, J. M. Jackson, W. Sturhahn and B. Chen, *Geophys. Res. Lett.*, 2011, **38**, L24306.

[87] S. Liu, J. Wei and F. Gan, *Applied Physics Letters*, 2012, **100**, 111903.

[88] K. S. Singwi and A. Sjölander, *Phys. Rev.*, 1960, **120**, 1093–1102.

[89] T. L. Anderson and H. B. Krause, *Acta Crystallographica Section B*, 1974, **30**, 1307–1310.

[90] T. H. K. Barron, W. T. Berg and J. A. Morrison, *Proceedings of the Royal Society of London. Series A. Mathematical and Physical Sciences*, 1957, **242**, 478.

[91] R. M. Nicklow, G. Gilat, H. G. Smith, L. J. Raubenheimer and M. K. Wilkinson, *Phys. Rev.*, 1967, **164**, 922–928.

[92] L. S. Salter, *Advances in Physics*, 1965, **14**, 1–37.

[93] S. Raoux, D. Ielmini, M. Wuttig and I. Karpov, *MRS Bulletin*, 2012, **37**, 118–123.

[94] G. Bruns, P. Merkelbach, C. Schlockermann, M. Salinga, M. Wuttig, T. D. Happ, J. B. Philipp and M. Kund, *Appl. Phys. Lett.*, 2009, **95**, 043108.

[95] K. Andrikopoulos, S. Yannopoulos, A. Kolobov, P. Fons and J. Tominaga, *Journal of Physics and Chemistry of Solids*, 2007, **68**, 1074–1078.

[96] R. De Bastiani, A. M. Piro, M. G. Grimaldi, E. Rimini, G. A. Baratta and G. Strazzulla, *Applied Physics Letters*, 2008, **92**, 241925.

[97] P. Němec, V. Nazabal, A. Moreac, J. Gutwirth, L. Beneš and M. Frumar, *Materials Chemistry and Physics*, 2012, **136**, 935–941.

[98] W.-P. Hsieh, P. Zalden, M. Wuttig, A. M. Lindenberg and W. L. Mao, *Applied Physics Letters*, 2013, **103**, 191908.

[99] P. Zalden, K. S. Siegert, S. Rols, H. E. Fischer, F. Schlich, T. Hu and M. Wuttig, *Chem. Mater.*, 2014, **26**, 2307–2312.

[100] T. Matsunaga and N. Yamada, *Phys. Rev. B*, 2004, **69**, 104111.

[101] B. Cordero, V. Gomez, A. E. Platero-Prats, M. Reves, J. Echeverria, E. Cremades, F. Barragan and S. Alvarez, *Dalton Trans.*, 2008, 2832–2838.

[102] K. A. Agaev and A. G. Talybov, *Sov. Phys. Crystallogr.*, 1966, **11**, 400.

[103] P. Bauer Pereira, I. Sergueev, S. Gorsse, J. Dadda, E. Müller and R. P. Hermann, *Phys. Status Solidi B*, 2013, **250**, 1300–1307.

[104] S. Caravati, M. Bernasconi, T. D. Kühne, M. Krack and M. Parrinello, *Journal of Physics: Condensed Matter*, 2009, **21**, 255501.

[105] G. Sosso, S. Caravati, R. Mazzarello and M. Bernasconi, *Phys. Rev. B*, 2011, **83**, 134201.

[106] A. I. Chumakov *et al.*, *Phys. Rev. Lett.*, 2014, **112**, 025502.

[107] B. Kalkan, S. Sen, J.-Y. Cho, Y.-C. Joo and S. M. Clark, *Applied Physics Letters*, 2012, **101**, 151906.

[108] A. van de Walle and G. Ceder, *Rev. Mod. Phys.*, 2002, **74**, 11–45.

[109] B. Fultz, *Progress in Materials Science*, 2010, **55**, 247–352.

[110] K. Ohara, L. Temleitner, K. Sugimoto, S. Kohara, T. Matsunaga, L. Pusztai, M. Itou, H. Ohsumi, R. Kojima, N. Yamada, T. Usuki, A. Fujiwara and M. Takata, *Adv. Funct. Mater.*, 2012, **22**, 2251–2257.

[111] N. Yamada, E. Ohno, K. Nishiuchi, N. Akahira and M. Takao, *Journal of Applied Physics*, 1991, **69**, 2849–2856.

[112] W. P. Risk, C. T. Rettner and S. Raoux, *Applied Physics Letters*, 2009, **94**, 101906.

[113] S. Caravati, M. Bernasconi, T. D. Kühne, T Dhne, M. Krack and M. Parrinello, *Applied Physics Letters*, 2007, **91**, 171906.

[114] P. Jovari, I. Kaban, J. Steiner, B. Beuneu, A. Schöps and M. A. Webb, *Phys. Rev. B*, 2008, **77**, 035202.

[115] R. Mazzarello, S. Caravati, S. Angioletti-Uberti, M. Bernasconi and M. Parrinello, *Phys. Rev. Lett.*, 2010, **104**, 085503.

[116] J. Akola, J. Larrucea and R. O. Jones, *Phys. Rev. B*, 2011, **83**, 094113.

[117] M. Krbal, A. V. Kolobov, P. Fons, K. V. Mitrofanov, Y. Tamenori, J. Hegedüs, S. R. Elliott and J. Tominaga, *Applied Physics Letters*, 2013, **102**, 111904.

[118] A. Pirovano, A. Lacaita, A. Benvenuti, F. Pellizzer and R. Bez, *Electron Devices, IEEE Transactions on*, 2004, **51**, 452–459.

[119] D. Ielmini, A. Lacaita and D. Mantegazza, *Electron Devices, IEEE Transactions on*, 2007, **54**, 308–315.

[120] I. V. Karpov, M. Mitra, D. Kau, G. Spadini, Y. A. Kryukov and V. G. Karpov, *Journal of Applied Physics*, 2007, **102**, 124503.

[121] J.-Y. Raty, W. Zhang, J. Luckas, C. Chen, R. Mazzarello, C. Bichara and M. Wuttig, Nature Communations, (2014), in review.

[122] M. Boniardi and D. Ielmini, *Applied Physics Letters*, 2011, **98**, 243506.

[123] D. T. Cromer and J. B. Mann, *Acta Crystallographica Section A*, 1968, **24**, 321–324.

[124] R. E. Simon, I. Sergueev, I. Kantor, A. Kantor, J. Perßon and R. P. Hermann, *Semiconductor Science and Technology*, 2014, **29**, 124001–.

[125] J. Kalb, F. Spaepen, T. P. Leervad Pedersen and M. Wuttig, *Journal of Applied Physics*, 2003, **94**, 4908–4912.

[126] S. Rols, H. Jobic and H. Schober, *Comptes Rendus Physique*, 2007, **8**, 777–788.

[127] V. F. Sears, *Neutron News*, 1992, **3**, 26–37.

[128] S. Buller, B. Dietl, J. van Eijk, P. Zalden, E. Welter, M. Wuttig and W. Bensch, *DESY Annual Report*, 2008.

[129] B. Huang and J. Robertson, *Phys. Rev. B*, 2010, **81**, 081204.

[130] G. Lucovsky and R. M. White, *Phys. Rev. B*, 1973, **8**, 660–667.

[131] D. Lencer, M. Salinga, B. Grabowski, T. Hickel, J. Neugebauer and M. Wuttig, *Nat Mater*, 2008, **7**, 972–977.

[132] T. Matsunaga, J. Akola, S. Kohara, T. Honma, K. Kobayashi, E. Ikenaga, R. O. Jones, N. Yamada, M. Takata and R. Kojima, *Nat Mater*, 2011, **10**, 129–134.

[133] J. Akola and R. O. Jones, *Phys. Rev. B*, 2007, **76**, 235201.

[134] J. Akola and R. O. Jones, *Journal of Physics: Condensed Matter*, 2008, **20**, 465103.

[135] J. Akola, R. O. Jones, S. Kohara, S. Kimura, K. Kobayashi, M. Takata, T. Matsunaga, R. Kojima and N. Yamada, *Phys. Rev. B*, 2009, **80**, 020201.

[136] T. Matsunaga, N. Yamada and Y. Kubota, *Acta Crystallographica Section B*, 2004, **60**, 685–691.

[137] T. Matsunaga, R. Kojima, N. Yamada, K. Kifune, Y. Kubota, Y. Tabata and M. Takata, *Inorg. Chem.*, 2006, **45**, 2235–2241.

[138] S. Sen, T. G. Edwards, J.-Y. Cho and Y.-C. Joo, *Phys. Rev. Lett.*, 2012, **108**, 195506.

[139] T. Matsunaga, Y. Umetani and N. Yamada, *Phys. Rev. B*, 2001, **64**, 184116.

[140] G. Alonzo, L. Garbato, F. Ledda and C. Muntoni, *Journal of Physics and Chemistry of Solids*, 1989, **50**, 1195–1196.

[141] K. Deneke and A. Rabenau, *Z. anorg. allg. Chem.*, 1964, **333**, 201–208.

[142] T. Schröder, T. Rosenthal, S. Grott, C. Stiewe, J. de Boor and O. Oeckler, *Z. anorg. allg. Chem.*, 2013, **639**, 2536–2541.

[143] J. Los, T. D. Kühne, S. Gabardi and M. Bernasconi, *Phys. Rev. B*, 2013, **88**, 174203.

[144] M. Takeda, M. Takahashi, Y. Yanagida, S. Kojima, K.-Y. Akiba and Y. Ito, *Hyper*, 1994, **84**, 439–446.

[145] P. Atkins, *Shriver and Atkins' Inorganic Chemistry*, OUP Oxford, 2010.

[146] F. Menil, *Journal of Physics and Chemistry of Solids*, 1985, **46**, 763–789.